The Dissertation Committee for Suenne Kim Certifies that this is the approved version of the following dissertation:

I-V Transport Measurements of a Single Unsupported MWCNT under Various Bending Deformations

Committee:

Alejandro L. De Lozanne, Supervisor

Arumugam Manthiram

James Erskine

Li Shi

Maxim Tsoi

I-V Transport Measurements of a Single Unsupported MWCNT under Various Bending Deformations

by

Suenne Kim, B.S.; M.S.

Dissertation

Presented to the Faculty of the Graduate School of

The University of Texas at Austin

in Partial Fulfillment

of the Requirements

for the Degree of

Doctor of Philosophy

The University of Texas at Austin

May 2008

To my parents, Jong-Jean Kim and Young-Sook Hong

Acknowledgements

First of all, I would like to thank and praise the Lord for shepherding me in love.

I thank my supervisor, Alex for all his supervisory arrangement and prayers. I've been put into many circumstances, which I can now appreciate it all for making me mature. He wasn't merely a supervisor but also a mentoring person with big and warm heart. Muchas Gracias~! I thank all of the proud committee, Prof. Arumugam Manthiram, Prof. James Erskine, Prof. Li Shi, and Prof. Maxim Tsoi. I appreciate their valuable time, advice, and warm hands of encouragements. I would not forget my great coworkers: Dr. Jeehoon Kim the devoted worker, Dr. Ayan Guha with amazing personality and Prof. Weida Wu the active one. I also can't forget each of my current and previous lab mates who made me feel comfortable in this foreign country.

I want to give my special thanks to the saints in Austin, Mickey, Sunmi, Nora, Mary, Youngseon & Jiseon, Bill & Camilla, Hara, Evelyn, Innah, Joanne, Henna, Faith, Yuko, Ruth and many important others for making my life meaningful and more fruitful. I also thank Dr. JaeHyuk Choi & Dr. HyunJung Park, and Dr. Soyeon Park & Dr. Yong Lee ringing in my heart.

I-V Transport Measurements of a Single Unsupported MWCNT under Various Bending Deformations

Publication No._____

Suenne Kim, Ph.D.

The University of Texas at Austin, 2008

Supervisor: Alejandro L. De Lozanne

The first part of this dissertation is an introduction describing a brief historical background of carbon nanotubes (CNTs) and their pseudo 1D structure responsible for many exotic electronic properties. The second part describes our experimental setup. The third part is about the growing of Multi-Walled Carbon Nanotubes (MWCNTs) by the chemical vapor deposition (CVD) method. Then the fourth part demonstrates a simple but reliable method to make firm contact junctions between MWCNTs and metals such as tungsten (W). The novel point of our method consists, after making a mechanical preliminary contact at a selected MWCNT, in applying a series of voltage pulses across the contact. Thin oxide layers that may form between the MWCNT and the W wire, are removed in steps by the resistive heating and electron impact during the application of each voltage pulse. Furthermore, this simple process of contact welding in steps does not bring about any permanent change in the electronic transport properties of the MWCNTs. The fifth part discusses our bending experiments. We apply a uniform and continuous bending to a selected MWCNT at room and liquid nitrogen temperatures to study the

strain effect on the electrical transport in the MWCNT. There are a few published experimental works related to the bending deformation; however, this is the first study of electronic transport properties in continuous bending and releasing deformations. We observed a saturation behavior with the MWCNT and also found the bending deformation causing an anomalous change in the saturation behavior. In the sixth part we depict some interesting phenomena due to the stretching deformation of MWCNT, where we were able to propose a simple model for electron localization induced by the deformation. The last part deals with the formation of the "X-junction" between two MWCNTs. A strong X-junction can be formed simply by means of the e-beam inside the Scanning Electron Microscope (SEM). The X-junctions may form the basic elements of nano-electronic circuits such as various metal-insulator junctions, quantum dots, and similar devices.

Contents

List of Tables

List of Figures

Chapter 1

Introduction

1.1 BRIEF REVIEW ON CARBON NANOTUBES

Diamond and graphite, of great technical importance, are better known materials composed of only carbon atoms. These old bulk materials are distinctive by their unique crystalline structures, the diamond structure where each carbon atom is bonded to four neighbors by covalent bonds, and the layered graphite structure with the carbon atoms arranged in a hexagonal array in each layer.

It is quite recent that other stable solid-state structures composed of carbon atoms have been discovered. In 1991, Iijima using High-Resolution Transmission Electron Microscopy (HRTEM) could identify the nanometer size concentric microtubules to be called Multi-Walled Carbon Nano-Tubes (MWCNTs) [1]. Well before this observation of MWCNTs, Kroto and coworkers reported an epoch-making discovery of fullerenes in 1985 [2]. The hemispherical caps at the terminations of the CNTs are found to have the fullerene-structural shapes. Hence Smalley et al. came to a speculation that a single-walled carbon nanotube (SWCNT) might be a limiting case extension of the fullerene molecule [3].

1

A connection between the novel nanometer-sized carbon materials and the well known graphite can be derived from the graphene, a single atomic layer of the graphite. Theoretical hypothesis can construct the fullerenes and CNTs in various forms with many possible cuts of the graphene sheet. The first step for understanding about the SWCNTs may thus be a study on the structure and the corresponding energy bands in graphite and the 2D graphene.

1.2 STRUCTURE AND ENERGY BANDS OF CNTS

1.2.1 Structure of SWCNTs

A SWCNT can be formed by rolling up a graphene sheet into a seamless cylindrical tube. The circumferential wrapping-up direction of any SWCNT is expressed by the chiral vector C, which connects any two crystallographically equivalent sites on the 2D graphene lattice [4]. The resulting structures are classified into three distinct types, depending on their chiral vectors which are so defined in terms of two 2D hexagonal lattice unit vectors, a_1 and a_2, as shown in Figure 1.1 [3].

$$\vec{C} = m \times \vec{a_1} + n \times \vec{a_2} \tag{1.1}$$

The sets of two integers, (m, n), represent the chirality of the nanotubes. The C, C', and C'' of Figure 1.1 each represent a respective example of the three distinct types. The chiral vector C gives a zigzag type, C' a chiral type, and C'' an armchair configuration.

We can define the chiral angle, θ so that the zigzag chiral vector gives the $\theta = 0°$ reference line and the armchair chiral vector lying at an angle of 30°.
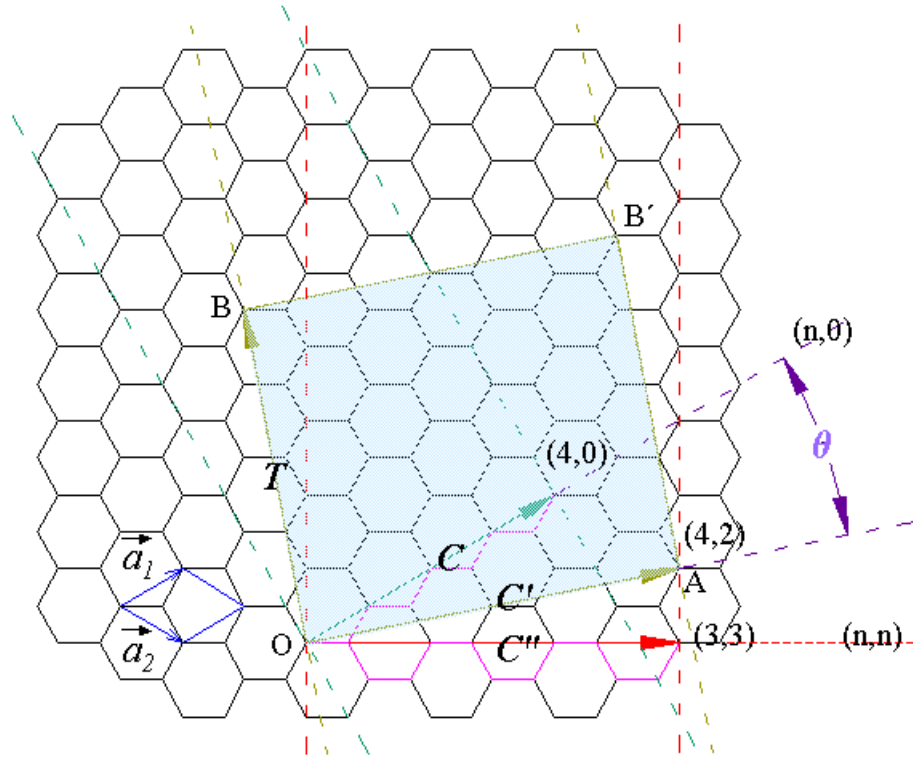
Figure 1.1: Geometrical parameters in construction of CNTs from the graphene sheet (Refer to [3]).

We show here how we go about constructing the (4,2) chiral CNT. We choose a chiral vector C' and a T vector perpendicular to the vector. The two end points, O and B, of the T vector are crystallographically equivalent to each other. The unit cell of the 1D lattice is the rectangle defined by the vectors C' and T [3]. When we imagine to make the nanotube by rolling-up along the chiral vector, the joint seam of the nanotube cylinder

will be aligned with the overlap line between OB and AB' of Figure 1.1. The final result for the (4,2) chiral CNT is then obtained as shown in Figure 1.2.
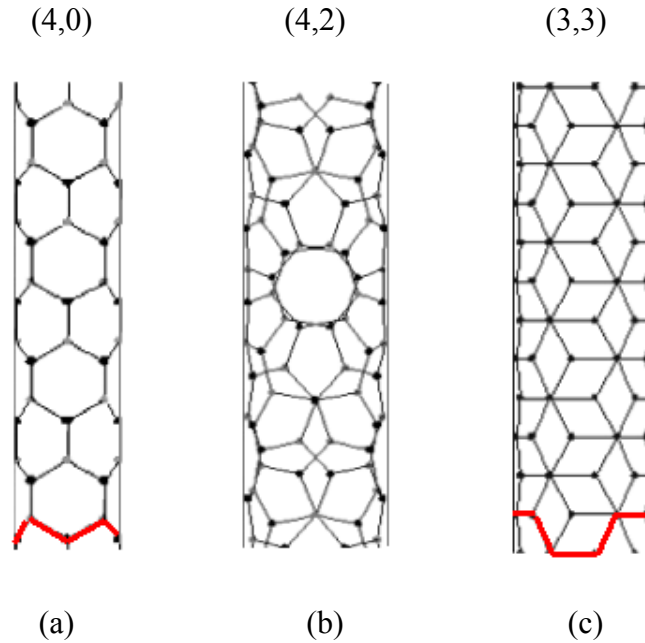
Figure 1.2: Schematic drawings for various types of SWCNT. (a) "zigzag" (4,0) nanotube, (b) "chiral" (4,2) nanotube, (c) "armchair" (3,3) nanotube.

From the definition of the chiral vector, the diameter of any CNT can be estimated as below and the ensuing differences in diameters between the selected chiralities of SWCNTs are shown in Figure 1.2.

$$d = \frac{C}{\pi} = \frac{a_{c-c}\sqrt{3}}{\pi}\sqrt{m^2 + n^2 + mn} \qquad (1.2)$$

where a_{c-c} is the nearest-neighbor C-C distance.

A SWNT becomes metallic if the value of n - m is divisible by 3 [3]. Otherwise, the nanotube is semiconducting. Consequently, when tubes are formed with random values of n and m, we would expect that two-thirds of nanotubes would be semi-conducting, while the other one third would be metallic.

1.2.2 Energy bands of CNT [5]

A carbon atom C has 6 electrons ($1s^2$ $2s^2$ $2p^2$). The outer shell 4 electrons (2 electrons in the filled 2s orbital and two electrons in the 2p orbital) of the isolated carbon atom C can be incorporated to form various 2D sp^2 or 3D sp^3 hybridized orbitals, depending on the respective underlying crystal structure of graphite or diamond.
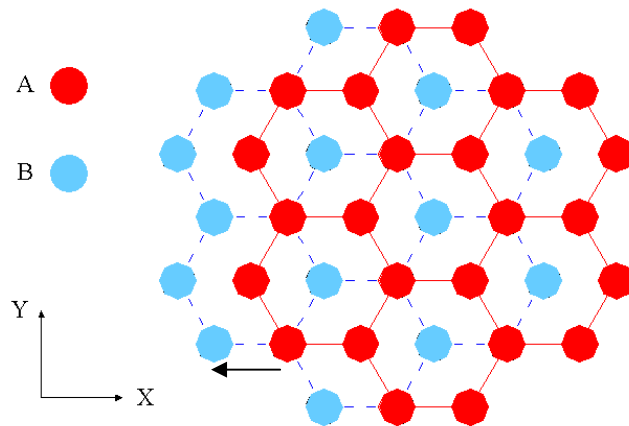
Figure 1.3: Schematic drawings for two adjacent layers in the ABAB… stacking of graphite structures. The bottom lower (blue) layer is offset from the top upper (red) layer in the –x direction by 1.42 Å (corresponding to the nearest-neighbor distance).

The crystal structure of graphite consists of parallel sheet layers of carbon atoms in the ABAB…stacking sequence as shown in Figure 1.3. In graphite, one s orbital and

5

two p orbitals undergo a sp^2 hybridization. The bonding geometry of the hybridized orbital is of a trigonal plane. This is the reason why each carbon atom within graphite has three nearest neighbors within the sheets. The remaining p (p$_z$) orbital overlaps with other p$_z$ orbitals of neighboring atoms to form the distributed π bonds that reside above and below each graphite sheet so that the layers are linked by weak Van der Waals forces of attraction.

For the graphene, also 3 electrons of sp^2 hybrid orbitals from each carbon atom form σ bonds with 3 nearest neighbors of the hexagonal lattice and electrons occupying the p$_z$ orbitals would overlap contributing to the itinerant π electrons. The uppermost one of valence bands is the π band and the bottom lowest one of the conduction bands is the $\pi*$ band. The σ valence band and $\sigma*$ conduction band would lie so far below and above the Fermi energy level that they may not interfere directly with the transport properties.

Figure 1.4 (a) shows the 1st Brillouin zone of the 2D graphene and it has 2 itinerant π electrons per unit cell. These are the actual electrons partaking in the electrical conduction. Some important high-symmetry points of Γ, K and M are designated with the 1st Brillouin zone in Figure 1.4 (a) [5]. The 2D energy dispersion relation near the Fermi level can be obtained on the basis of a tight-binding calculation for the π and $\pi*$ bands around the Fermi level from the p$_z$ orbitals of the graphene sheet [5].

$$\varepsilon(k) = \pm\beta_{pz} \sqrt{1 + 4\cos\{\frac{\sqrt{3}k_x a}{2}\}\cos\{\frac{k_y a}{2}\} + 4\cos^2\{\frac{k_y a}{2}\}} \qquad (1.3)$$

where β_{pz} is the nearest-neighbor overlap integral for p$_z$ orbitals.

We can see from Figure 1.4 (b) that the conduction band and the valence band are degenerated at the K point to give a zero gap with the vanishing density of states at the

6

Fermi level as responsible for the graphene to become a semimetal, while M point yields a finite gap and the Γ point has a larger gap [5].

(a)
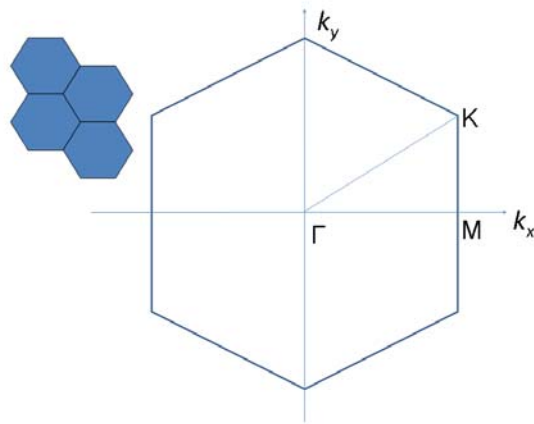
(b)
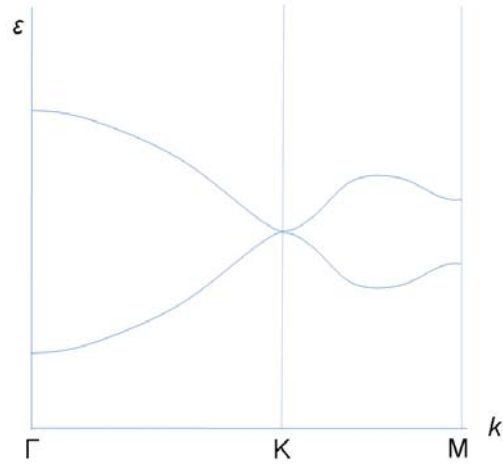
Figure 1.4: (a) 1st Brillouin zone with Γ, K, and M high-symmetry points. (b) The conduction and the valence bands in the Γ-K-M direction of κ-space near the Fermi level at the K-point degeneracy for 2D graphene.

The itinerant π electrons play an important role also with the CNT. The electronic band structure of a SWCNT can be constructed by the zone folding modification of the dispersion relation for the graphene as given by the periodic boundary condition around the cylindrical tube circumference.

1.2.3 MWCNT

Some HRTEM images of the concentric microtubules, MWCNTs, are shown in Figure 1.5 [1].
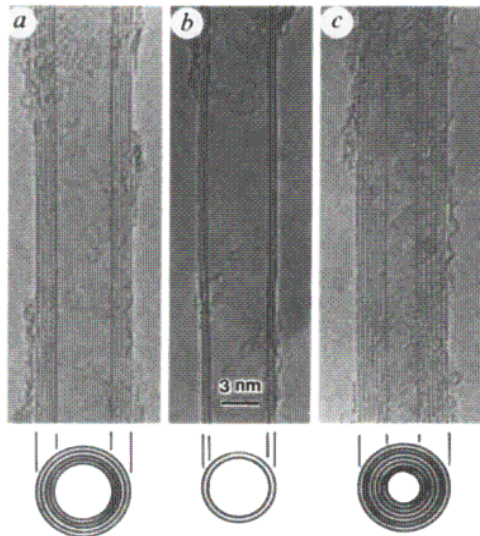
Figure 1.5: TEM images of MWCNTs (from [1]).

Despite successful applications of MWCNTs, transport properties of MWCNTs are not well understood and even controversial between ballistic and diffusive conduction

8

behaviors in contrast to the case of SWCNTs with the ballistic conduction behavior as confirmed by many theoretical and experimental studies.

MWCNTs have very complex electronic band structures near the Fermi level to complicate their transport properties. For example, for the most common incommensurate concentric MWCNTs it becomes very confusing to count the number of conductance channels to be used in the Landauer's formula for the ballistic conduction due to different (incommensurate) periodicities for different shells of the MWCNTs.

1.3 ENERGY BAND MODULATION OF CNT

Also theoretical studies have been reported that flattening deformation drastically changes the metallic properties or band gap of the original nanotubes into very different electronic properties. Breaking of the mirror symmetries by flattening, in the metallic armchair nanotubes may lead to a finite band gap at the original degenerate Fermi level, that is, metal to semiconductor transition [6, 7]. Semiconductor nanotubes on the other hand can be transformed to be metallic when they are forced to collapse down to an interlayer spacing of 3.35 Å [8].

Figure 1.6 shows a typical case of bending deformation with a SWCNT and the accompanying changes in the local electronic density of states (DOS) as obtained from the tight-binding approximation. The Fermi level is located by a box of pink lines. The top frame represents the result from the unstrained nanotube and the middle one is of the bent nanotube. The local DOS can be seen to increase with the bending deformation.

 Long CNTs are very strong but flexible so that various deformations may be produced easily with very large reversible deformations beyond the normal elastic limit.

Band-gap modulations of the MWCNTs by bending and other deformations will be studied to find out the most efficient ways of applying stress to control for reversible or irreversible electronic band-gap modulations, where a close examination will be also made about possible hysteresis loops of irreversibility in the electronic transport properties associated with the deformation.
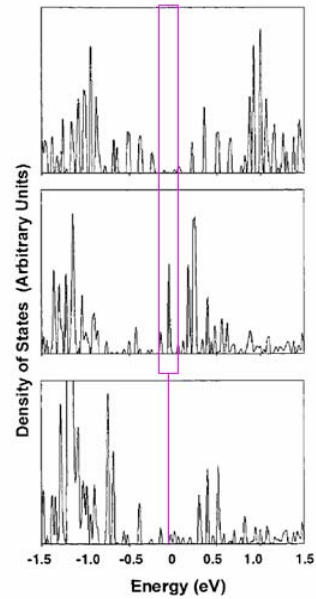
Figure 7. Local electronic density of states from the tight-binding model for the reactive carbon atom at the top of the kink discussed in the text. The Fermi energy is at zero. Top: Unstrained nanotube. Middle: Bent nanotube before hydrogen chemisorption. Bottom: Bent nanotube after hydrogen chemisorption to this site.

Figure 1.6: Density of states (DOS) changing with the bending deformation in CNT [9].

Such efforts of innovations have been driving the carbon nanotubes to be emerging in the last decade as an ideal material for the building block of the forthcoming nanotechnology. Here we would like to add some useful details from our transport measurements on CNT junctions relevant to a novel functional device intrinsic to the CNTs.

1.4 CNTs in Basic Science and Applications

Applications of CNTs are so numerous in various fields of science and engineering from high precision nanoscopic probe resolution to heavy industrial products. To give an idea for the trends of research and development (R & D) with the 21C industrial applications of CNTs, we may well sample a few illustrations as follows based on [10] and [11]. First, terra-range super high-density integration of memory chips in lieu of the current Si memory chips. Second, electrode materials for secondary battery cells or fuel cells that use the ultra low weight, environmental and chemical stability, excellent capacity for hydrogen storage, etc. Third, STM or AFM probe tip with excellent electrical conductivity and super mechanical rigidity for hyperfine structural imaging with nano-resolution or local site microscopic information. Fourth, in conjunction with nano bio-technology (BT) developments of hyperfine connection wires for biological structures, hyperfine pipelines for bio-doping or bio-injection, hyperfine medical accessories making use of compatibility with biological structures, etc. Fifth, nano-probing with gas sensors that make use of the CNTs' excellent adsorption efficiency for gases. Lastly, as a raw component element of the composite materials for bulletproof fiber materials, electromagnetic wave shielding, industrial wrapping sheets, and device elements for field emission displays.

Chapter 2

Experimental Setups of the SEM Works and Improvement in Low Temperature Probe

2.1 SYSTEM SETUPS IN THE SEM

Making a single CNT at the end of a chemically etched W tip by chemical vapor deposition (CVD) is painful and time consuming. Usually it takes a month to get a right length CNT-W tip for the CNT bending experiment in this way, and the CNTs are usually not straight. We need to make the CNT-W tips in a consistent and reproducible way for the CNT bending and extending experiments of the thesis work.

Therefore we have developed the CNT-W tip-making system inside our Scanning Electron Microscope[1] (SEM) shown in Figure 2.1. The CNT-tip making system mainly consists of an X-Y-Z (3D) walker, a scanner tube, an anode and a cathode. The electrodes are used to apply pulses to remove an oxide layer between a single CNT and an etched W wire in welding, and to do the transport measurements in the bending experiments. The mechanism for the welding is examined in chapter 4 in detail.

The Attocube[2] design is adopted for the 3D walker. A stainless-steel slider holding a graphite rod slides up or down depending on the waveform of a saw-tooth

---

[1]JEOL JSM-820

[2]Omicron Nanotechnology, Patent number: 5,912,527

12

voltage. The stainless-steel slider is not stuck even at low temperature because of the graphite rod, which acts as a lubricant. One can choose titanium for a slider for the high magnetic field experiment instead of stainless steel. The working principle of the walker is illustrated in Figure 2.2.
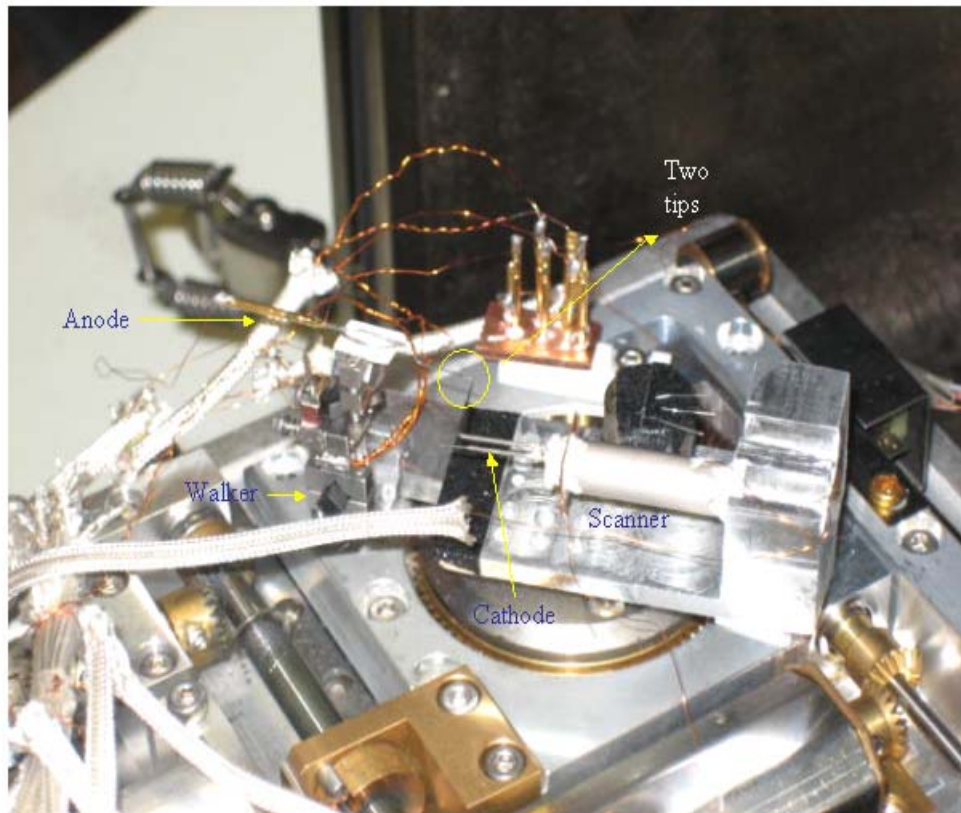
Figure 2.1:   Setup inside the SEM. All the main parts are named with the blue lettering.

A W-tip on a slider is getting close to a sample surface as a piezo-stack[3] expands by increasing the voltage [that is from (a) to (b) in Figure 2.2 (d)] supplied to the stack. A

---

[3]Tokin Co. Model number: AE0203D08

slider stays due to the inertial force while a piezo-stack suddenly contracts by decreasing the voltage [that is from (b) to (c) in Figure 2.2 (d)] suddenly. By this inertial mechanism one can approach the tip to the sample surface or retract it from the surface.
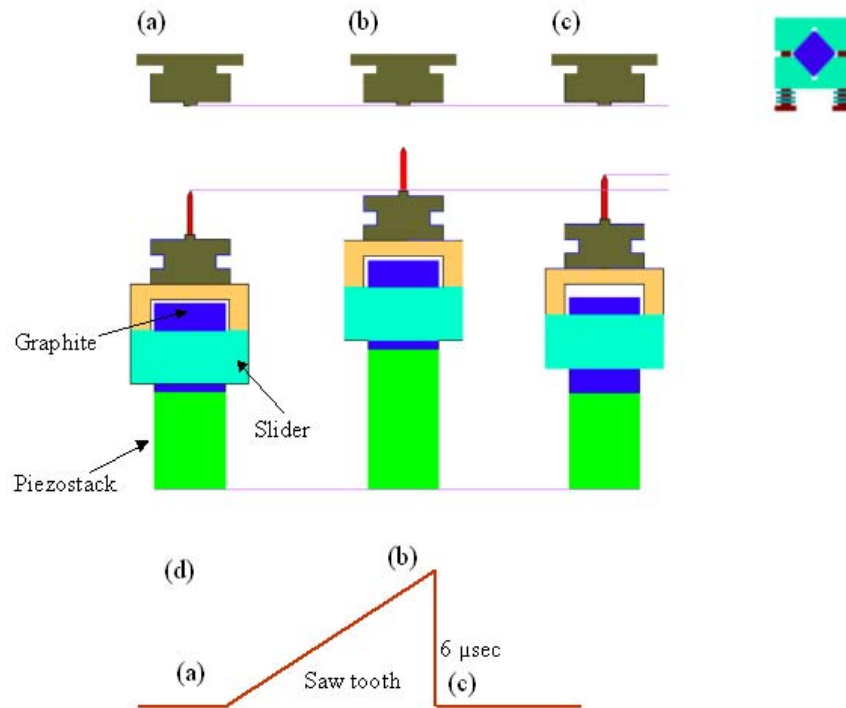
Figure 2.2:   Attocube mechanism (courtesy of Jeehoon Kim).

There are two important parameters to make the Attocube work efficiently, even at a low temperature. Both a longer travel distance of piezo-stack and a shorter transition time of the falling edge of a saw-tooth waveform result in the increase of the inertial force, which is essential for operating at a low temperature.

2.2 PROBE DESIGN

We adopted STM approach mechanism to bring a CNT attached W-tip within 10 Å of the gold substrate. Our probe is designed to directly dip into liquid nitrogen. The first part of this section describes the approach mechanism we adapted from STM and the latter part is about our cold finger specially designed to satisfy two purposes: "smooth sliding in" and "good heat conduction".

2.2.1 STM Approach Mechanism and Data Acquisition
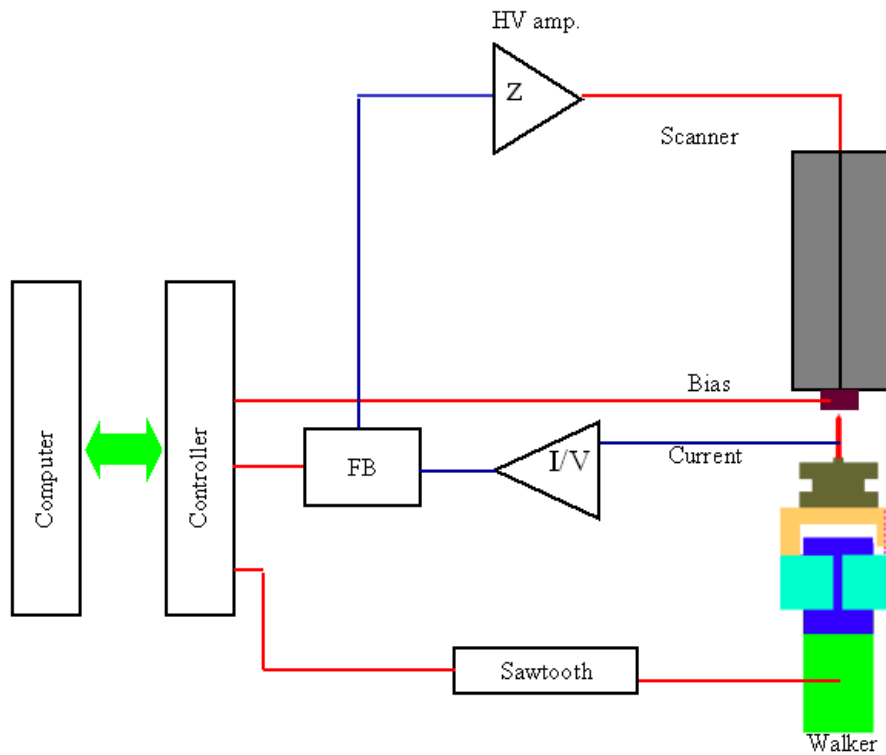
Figure 2.3:   STM approach mechanism (courtesy of Jeehoon Kim).

Figure 2.3 shows the basic principles involved in the approach mechanism of a STM system. This STM approach principle is employed to find a contact point when a carbon nanotube hits an Au thin film on mica. The whole system of our CNT-bending experiment is depicted in Figure 2.4.
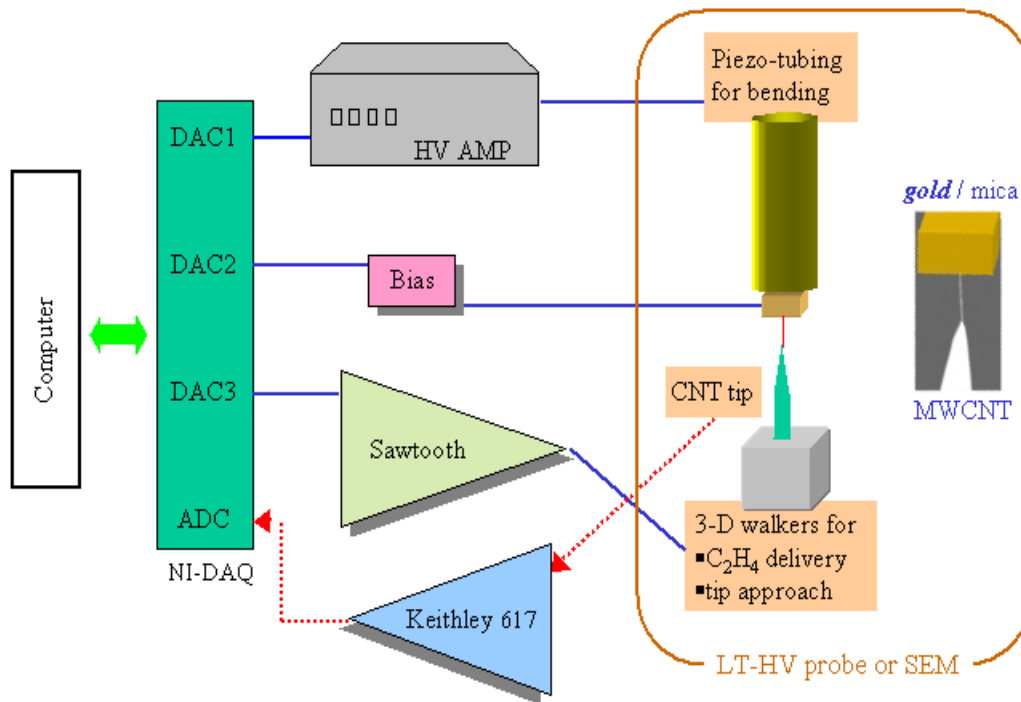
Figure 2.4:   System Setup for our CNT-bending and stretching experiments.

For the bending experiment, homebuilt walker, scanner, cathode, and anode are all installed in the SEM and the homemade low temperature high vacuum probe (LT-HV probe) respectively. The base pressure of the SEM measured by a cold cathode gauge is better than 10^{-5} Torr. Care should be taken in using a cold cathode gauge. It should be

installed away from the center of the chamber in the SEM so that it does not affect the e-beam path due to the stray magnetic field from the gauge.

A homebuilt X-Y-Z walker is used for a "coarse approach" having a minimum step size of 100 nm and able to travel up to 3 mm. The walker operates with the inertial mechanism as described previously, driven by a homebuilt saw-tooth generator. A 0.75-inch long PZT-5H[4] piezoelectric tubing with the outer diameter of 0.25 inch is used for the scanner as a fine approach. The scanner tubing has wall thickness of 0.02 inch. The travel distance of the piezo-scanner is larger than the minimum step size of the walker. This allows us to use the STM approach mechanism to bring the anode electrode (either an etched W wire or a CNT attached W-tip) to the cathode electrode (a single CNT or Au substrate) into the tunneling regime of less than 1 nm. A sharp Pt/Ir tip also can be used to attach a single CNT. It can be electrochemically etched in a 1M calcium chloride solution ($CaCl_2$) by applying an a.c. 25V bias. The etching procedure of the W wire is described in detail in the following chapter. CNTs grown on a 10-mil tungsten wire is inserted into the stainless syringe glued on the scanner tube. A NI-DAQ card is used to interface the homemade LabVIEW program with surrounding hardware such as a homebuilt high voltage amplifier, a programmable electrometer[5] and a homebuilt saw-tooth generator.

The principle of the STM operation is adopted to make contact between the anode and the cathode for the transport measurements. The piezoelectric scanner is expanding in steps of 0.1 nm up to 2 μm with the feedback on. The feedback is detecting the tunneling current in the STM. If the tunneling current is not detectable from the Au substrate to the CNT attached W-tip, the scanner goes back to its original position [in our

---

[4]EBL Products Inc. EBL#3
[5]Keithley 617

17

case, contracting by 2 μm]. Now the walker moves one-step up, the minimum step size is around 100 nm at room temperature, and the piezo-scanner expands again to find the tunneling current. This approach process is done over and over again until the tunneling current is obtained.

For the piezoelectric scanner in the LT-HV Probe, the travel distance at room temperature is ~3.2 μm.

This can be calculated by:

$$\Delta L = \frac{d_{31} \times V_{MAX} \times L}{t} \left(\text{Å} \right)$$

(2.1)

where d_{31} = -2.62 Å/V (300 K) and -0.92 Å/V (78 K), V_{MAX} = 200 V, t = 0.02 ″, and
L = 1.2 ″ (for the scanner in the LT-HV Probe)

  = 0.75 ″ (for the scanner in SEM)

so that we may obtain ΔL (300 K) = 3.2 μm (for the scanner in the LT-HV Probe)

        = 2 μm (for the scanner in SEM)

The I-V measurement in the SEM or in the LT-HV Probe starts by ramping up the bias voltage (forward-bias measurement) immediately after the tunneling current is obtained and the backward-bias measurement is performed right after completing the forward-bias measurement. By this measurement process, one can minimize the effect of the piezoelectric scanner hysteresis and confirm the acceptable data quality.

2.2.2 Cold Finger
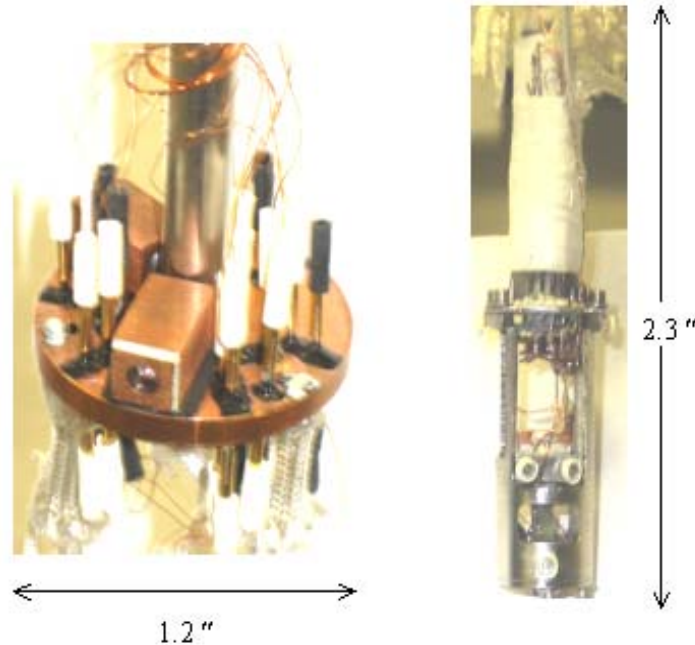
Figure 2.5: The cold finger on the left and the STM head including the piezoelectric scanner, Z walker on the right.

Our homemade cold finger is depicted in Figure 2.5. The head part is hung from the cold finger by springs as shown in Figure 2.6. The very effective low-k springs were designed to isolate the head from the environmental mechanical vibrations when used with fiber glass sleeves[6] for damping. The cold finger is tightly attached to the 0.25-inch stainless-steel inner tubing by mechanical force. All these parts are inserted to the outer jacket stainless-steel tubing as shown in Figure 2.6. As can be seen in Figure 2.6 the cold finger is directly touching the outer stainless-steel tubing and the tubing directly goes into cold cryogens (LN_2, LHe).

---

[6]Bentley Harris

19
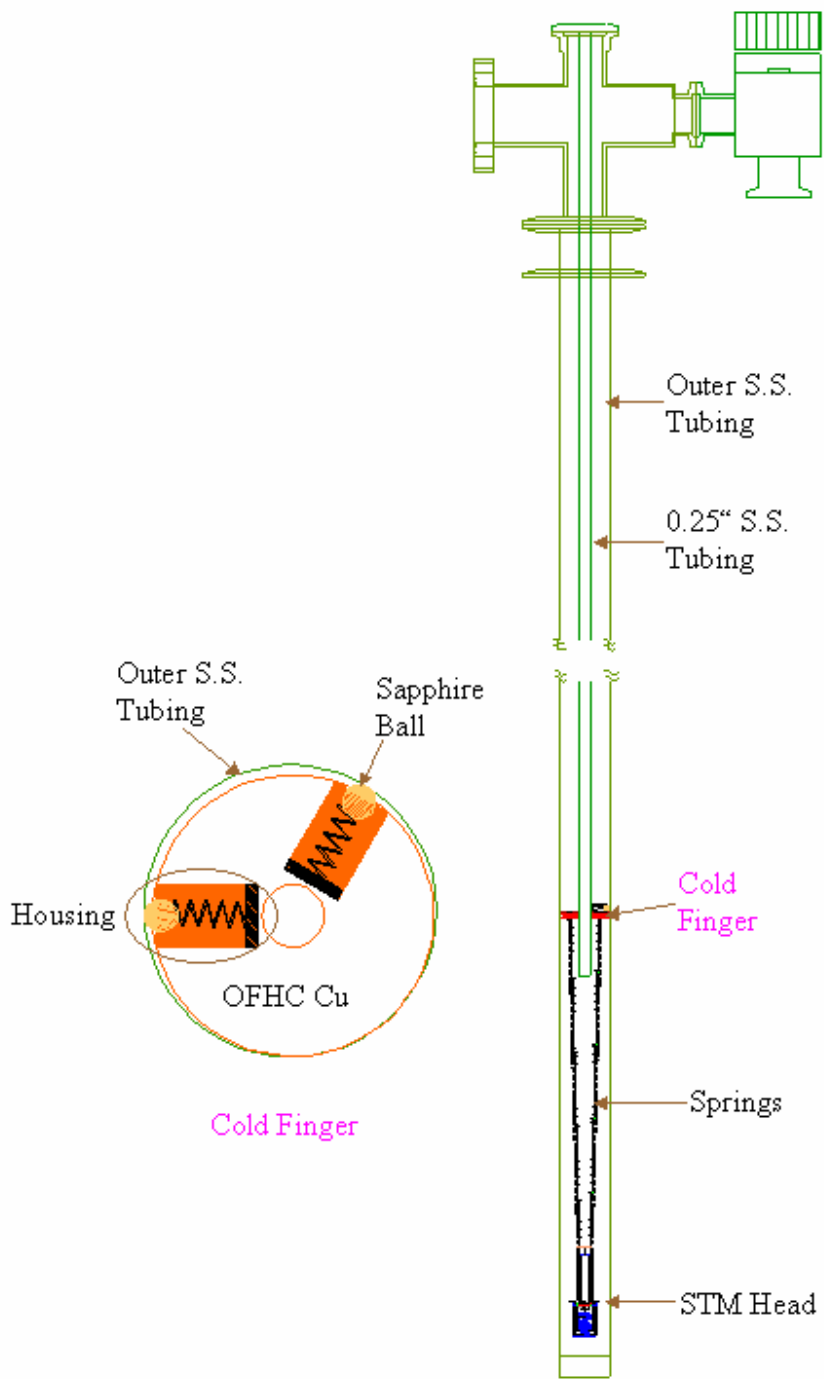
Figure 2.6: The low temperature high vacuum Probe.

Therefore it is important for the cold finger to satisfy two conditions. That is, "Being able to slide" to go in while it should have a good contact with the sliding surface (the stainless-steel outer tubing) to give a direct path for heat conduction. This incompatible situation can be solved by using a spring and sapphire ball combination. We used only two housings which contain a spring and a sapphire ball for each. This makes the two balls to push the Cu cold finger to the wall by the spring force allowing the third Cu contact as shown in the inset of Figure 2.6. So, there are 2 point-contacts made by the sapphire balls and a line-contact by the Cu finger for cooling.

There are two major heat energy carriers: electrons and phonons. The phonons may be more active at high temperatures while the electrons become the main heat carriers at low temperatures. Our homemade cold finger is working so well in the linear regime as to reach ~ 80 K within 30 minutes from 300 K at below 2 mTorr. Based on the data by Tomaru [12], sapphire is really a good heat transfer material better than pure Aluminum in the range of the temperature from 20 K to 100 K. This high thermal conductivity of sapphire explains its surprising heat transfer efficiency at low temperature.

Chapter 3

Synthesis and Preparation of CNT Samples

3.1 INTRODUCTION

In this chapter we describe various growing methods for CNTs including a short introduction about the methods of arc-discharge and laser ablation. These two methods were actively used in the early years. Then we discuss the Chemical Vapor Deposition (CVD) method, which we are using in the present work because of its easy and simple processing. Furthermore, it is so far the best way to grow CNTs directly on other substrate materials with less byproduct to make the method as unique and very useful.

Our preparation of the CNTs is aimed at studying their transport properties under the application of stress and making nano-probes for Scanning Probe Microscopy (SPM). The advantages of using CNTs as the SPM tips are due to CNTs' unique nanoscopic properties such as their high flexibility, good thermal stability, chemical inertness, good conductivity and high mechanical strength. The CNT diameters are in the range of 0.6-200 nm and their lengths vary from tenths of nanometers to millimeters [13]. In essence, they have the high aspect ratio and the nano-metric sharpness that are all the important qualifications for nanoscopic SPM tips. On the other hand, as for the use as SPM tips, CNTs also encounter some technical difficulties, such as vibrations of the CNT, poor

ohmic contact between the CNT and the metal tip, etc. The first problem enforces the requirement of shorter CNTs [14] and the second problem may be solved by our novel method of "serial pulse welding" as described in detail in chapter 4.

3.2 MECHANISMS FOR GROWTH OF CNTS

3.2.1 Arc-Discharge and Laser Ablation

The arc-discharge method was first used to grow fullerenes. The breakthrough in the growth of MWCNTs by this method was achieved by Ebbesen and Ajayan, who could produce high quality MWCNTs at the level of gram quantities [15]. The procedure requires two graphite rods to be connected to the arc-discharge power supply. The rods are set to be a millimeter apart, when the arc-discharge current of around 100 A vaporizes carbon to form hot plasma [13]. This produces short and small diameter CNTs with few structural defects but a lot of byproducts that need purification.

Laser ablation method was used to produce high quality SWCNTs at the scale of gram quantities by Smalley and coworkers [16]. This method uses intense laser pulses to ablate a graphite target and generate carbon gas with the target placed in a furnace heated to 1200 °C [16]. The team used a composite of graphite and metal catalyst particles to synthesis SWCNTs. This method may produce good quality SWCNTs with a good control of diameters determined by the reaction temperature but remains rather expensive.

3.2.2 Chemical Vapor Deposition

In this section we describe in details about our way of growing CNTs on etched W wire by CVD method. First, we need to make W-tips. We define here a W-tip by an etched W wire. As for an STM tip, W-tips must not be etched too sharp. Otherwise, the chance of growing one protruding CNT on the very summit end of a W-tip will be drastically reduced. Second, we need to coat the W-tip with chemical catalyst. Lastly, we need to flow a carbonaceous gas in stream over the W-tip at high temperatures.

Etching W wire
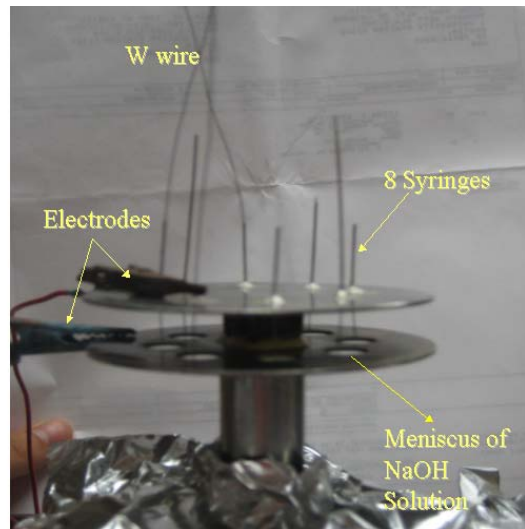
Figure 3.1: Device for etching wires for the STM probe tips (courtesy of Jeehoon Kim).

Figure 3.1 shows our etching setup ready for production. We can etch up to 8 wires at one time in one batch. The details of the whole procedure are as follows:

24

1) Cut a piece of 10-mil W wire to a length of 4 inches from the wire roll.

2) Straighten and clean the wire with ethyl alcohol just to remove visible debris, and then put it into the syringe tubing for etching.

3) Put a thin film of 2 M potassium hydroxide (KOH) or 2 M sodium hydroxide (NaOH) solution to make a meniscus as shown in Figure 3.1. The full etching time can be controlled by the thickness variation of the meniscus. If it is etched too fast, the resultant aspect ratio becomes too low. It is thus important to control the thickness in accordance with your own purposes. A silicon bar is good for making the meniscus because it does not react with the solution.

4) Apply a.c. or d.c. voltage of about 2-3 V between the two alligator clips connected to the respective electrode plate as shown in Figure 3.1. Lower the wires until passing through the meniscus. In case of the a.c. voltage application we must check for small bubbles ensuing around the wires. If no bubbles are observed, try to raise the voltage by a small step. The tips should be etched in ~15 mins.

5) When the bottom part falls off by the etching, then turn off the power. This timing for turning off is crucial to determine the sharpness of the etched tips. The shorter the timing interval is given, the sharper the tip becomes. It is shown by distinctive illustrations in Figure 3.2. Other important technical details can be found in the work of Allan [17].

Cleaning and electroplating with catalyst

This cleaning process uses hydrofluoric acid (HF), which is commonly used to
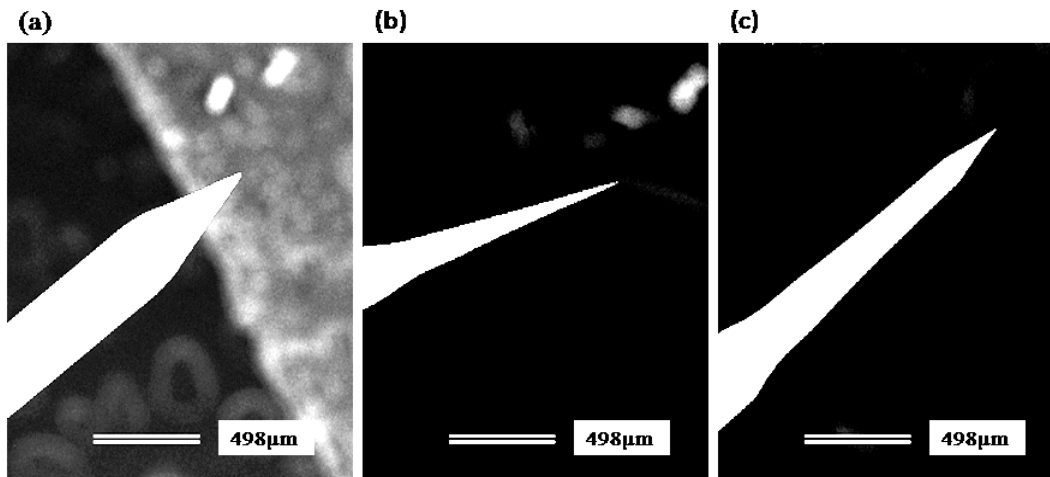
Figure 3.2: Results of the etched W-tips obtained by varying the voltage turning-off time: (a) ~3 sec, (b) 0.5 sec, (c) ~1 sec. [double dip etching in KOH solution leads to a corresponding change in the sharpening slope]

clean rusty metals. The time interval between the cleaning and the dipping of the tips into the catalyst is vital to determine the density of the nanotubes that are grown. If the procedure takes too long, the tips will be oxidized to drastically reduce the chance for catalyst atoms to stick at the surface sites. We are using a 2M solution of ferric nitride ($Fe(NO_3)_2$) for supplying catalyst atoms. We place the carbon (graphite) bar inside the solution to be used as one electrode. We apply a d.c. voltage of about 2 V from the power supply for half a second between the W-tip and the electrode in the solution to electroplate the tips with Fe ions. To grow a massive amount of CNTs on the sides of the W-tips, we can dip the W-tips directly into the catalyst solution for about 3 hours. However, it is also imperative to keep the time within the error bars of 10 minutes on the basis of our trial-and-error experiments. The difference can be appreciated from Figure 3.4 and Figure 3.5.

26
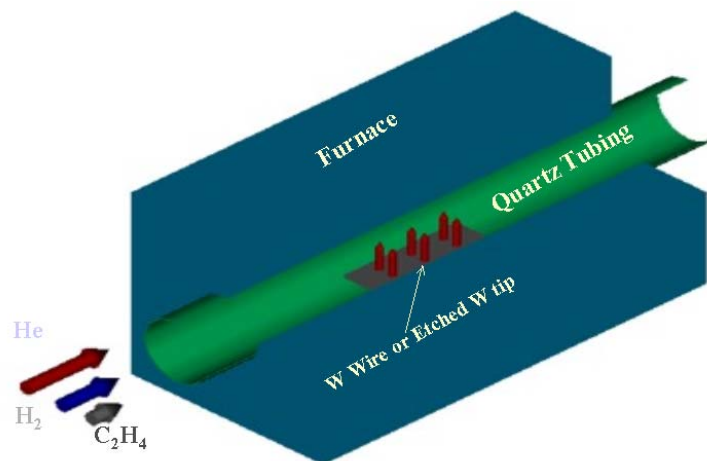
Figure 3.3: Furnace setup at high temperature to grow CNTs. (Courtesy of Jeehoon Kim)

Baking

Our setup of high temperature furnace for baking is shown in Figure 3.3. We start with flowing the helium (He) and hydrogen (H_2) gas. Helium flow should be controlled at a rate of 9.8 bubbles/second and hydrogen flow at 5.5 bubbles/second. The furnace is built to run by a program already set for this procedure. When the furnace reaches the temperature of 750 °C, we flow the ethylene gas (C_2H_4) for ~10 min. The ratios of flow rates between the different gas flows we used are set to He: H_2: C_2H_4 = 9.8: 5.5: 2.2. Cooling down the furnace is the next step. When the furnace is cooled down to a temperature below 100 °C (approximately 1 h and 30 min later), we may turn off the He gas flow because there will be no longer reactions with other mixing gases below this temperature. The CNTs can be then collected for examinations in the SEM. The results of our observations are shown in Figure 3.4. The diameters of our MWCNT samples are ranging from 5 to 25 nm and a typical TEM image is illustrated in Figure 3.6.
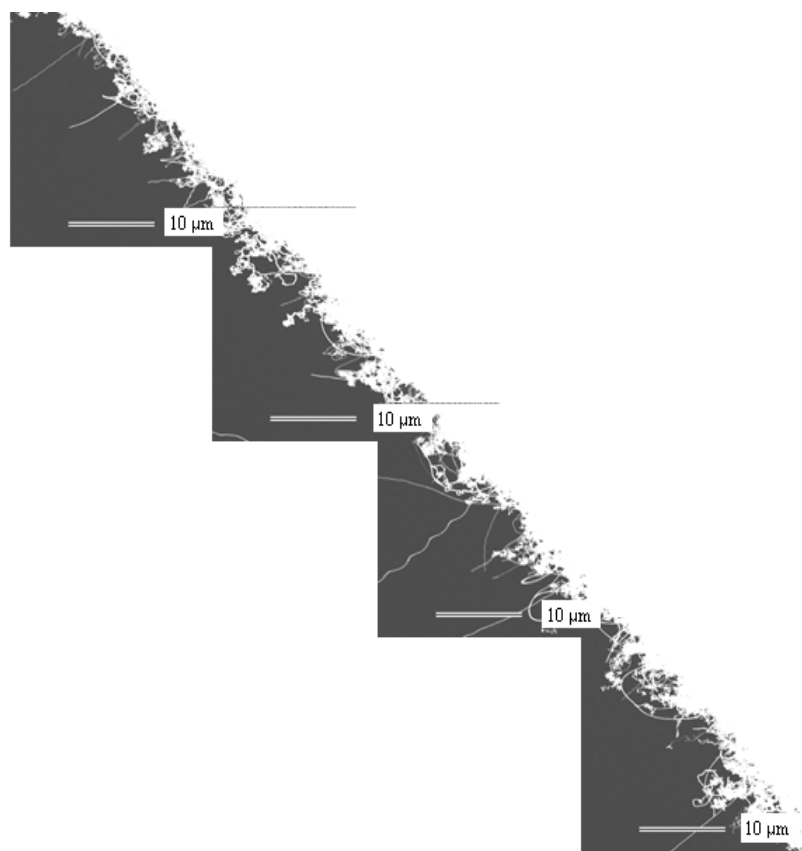
Figure 3.4: SEM image of the MWCNTs grown by the CVD method. The W-tip was dipped for 3 hours in the catalyst solution.
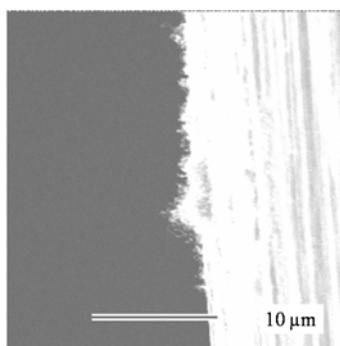
Figure 3.5: SEM image of the MWCNTs grown by the CVD method. The W wire was dipped in the catalyst solution for 2 hours.
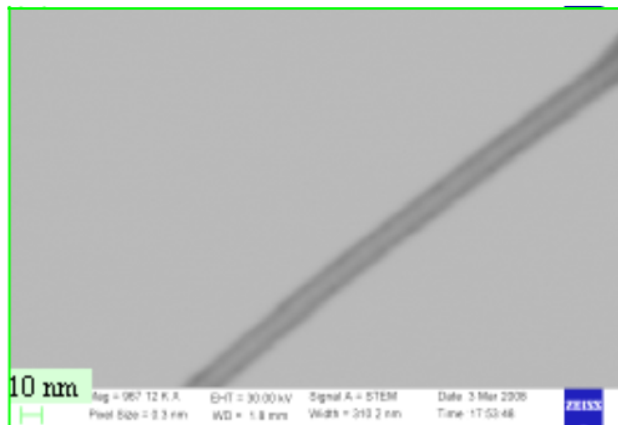
Figure 3.6: TEM image of a MWCNT grown by the CVD method.

3.3 GROWING MWCNTS OF HIGH QUALITY

We can find very high quality MWCNTS occasionally only in the restricted area of high curvature with the W wire as shown in Figure 3.7. We speculate that a porous area might develop when we bend the W wire before coating with catalyst. These pores might be able to act as nucleation sites for Fe ions or as catalytic pathways with minimal energy cost for nanotube growth. The CNTs grown in this way is easy to detach from the W wire unlike those in many other cases. This depends probably on the details of the growth mechanism. The catalyst particles can stay at the tips of the growing nanotube during the growth process, or remain at the nanotube base, depending on the adhesion between the catalyst particle and the substrate.

29
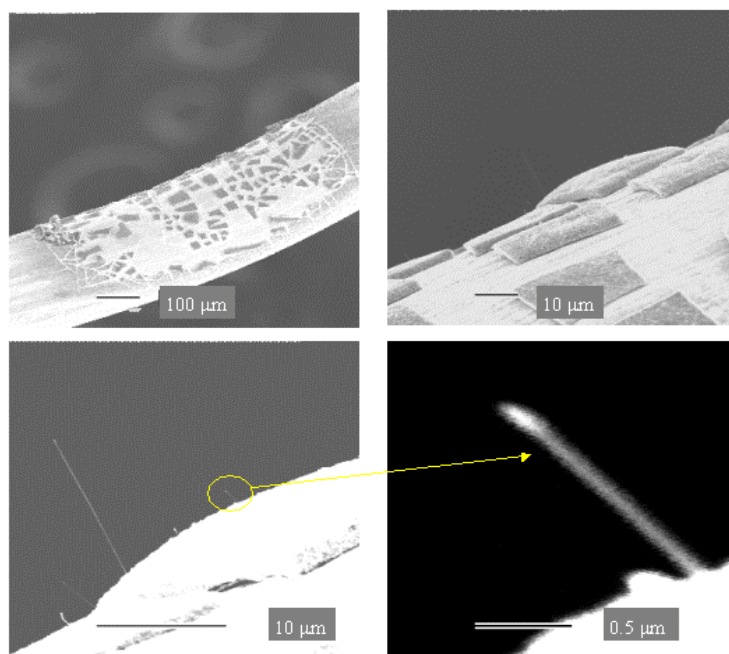
Figure 3.7: SEM images of the MWCNTs grown with the W-tip dipped for 3 hours in the catalyst solution.
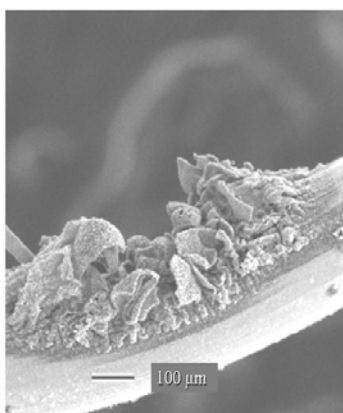
Figure 3.8: SEM image to show local structures of the thick catalyst layers formed at the bend.

This right condition is not easy to be achieved because it may be related to the local curvature at the bend, molar concentration of catalyst in the spot area, etc. as can be presumed from Figure 3.8.

3.4 CONCLUSIONS

We made use of the CVD method to grow our samples of CNTs on W wires. Further improvements are still needed for some control parameters to produce high quality CNTs. We suggest some issues in the following for further discussions.

The etching process does not seem to interfere much with the growth habit of the CNTs, although the blunt shape of the tips seems to help the growth site to be the very end of the tip. There are several factors that would affect the sharpness of the W-tips, of which we want to address the following three most important parameters. One is the thickness of the meniscus, another one is the partial length protruding below the meniscus, and the last factor of utmost importance is the voltage turning off time.

"Increasing the time interval between the cleaning and the dipping process" may degrade the adhesion of catalyst layers to reduce the probability for the rooted growing of CNTs. This result may be attributed to oxidation of the tips during this time interval, preventing the bonding of metallic atoms. However, we can control the density of the grown CNTs by adjustment of this time interval.

The W-tips placed on the sides of quartz tubing are often observed to give higher density of grown CNTs than those in the middle. We suspect that it may be related to the streamline distribution of the vapor flow. This problem is left for further studies to follow in the future.

31

Chapter 4

Fabrication of Metal Tip Bonding with a Multi-Walled Carbon Nanotube in Scanning Electron Microscope

4.1 INTRODUCTION

After its discovery by Iijima [1], the carbon nanotube (CNT) has been the most attractive material of science and engineering towards nanotechnology (NT) innovations in the last two decades. Both theoretical and experimental works have been able to find many low dimensional exotic properties expected from the quasi 1D structure of CNTs. Also the unique mechanical properties, coming from its extremely high axial stiffness but very easy radial deformation with a cylindrical tube shape structure of just the right nanometer-scale dimensions, made the CNTs most useful and promising for various commercial applications of the coming NT age.

CNTs have also been making a significant contribution to foster the basic research advances in mesoscopic science and engineering by realizations of the ultimate high resolution probe tips of scanning probe microscopy (SPM), nano-tube filling or doping variations inside the hollow cylindrical nano-shells [18, 19, 20, 21, 22, 23]. All these R & D (research and development) works need a reliable CNT bonding to metals. Thus if we find a simple way of making a stable bonding between CNT and other well-characterized

metals, we may expect a giant step forward to a new prosperous era of the numerous useful combination networks and NT-hybrid integration.

Here we want to show a simple and reliable method to make a very stable bonding of CNTs with easily affordable tungsten (W) wires with the utmost success rate, reaching almost 100%. We made the electronic transport measurements *in situ* to confirm the mechanically strong and electrically good contact of the CNT-W tip. We convinced ourselves from the experimental tests of the present work that our unique welding method for obtaining the ideal nano-contacts could be extended to other CNT applications with such strong bonding contacts as to withstand all the laboratory tests of engineering and technological applications.

4.2 TIP FABRICATION AND RELIABILITY TEST

For preparation of the CNTs to be used in our experiments we employed the catalytic chemical vapor deposition (CVD) method to synthesize our MWCNTs directly onto the surface of tungsten (W) wires. The process involves passing a gas flow of ethylene vapor for 10 minutes at 750 °C through a quartz-tubing furnace which contains the catalyst-deposited W wires. We used transition metal (Fe) catalyst to decompose the hydrocarbons. After getting enough concentration of randomly grown CNTs [Figure 4.1 (b)] we proceed to select and attach one CNT to the W wire by using scanning electron microscope (SEM) welding [24, 25]. The full procedures showing how we go for attaching the selected CNTs to the chemically etched W wire are depicted step by step in Figure 4.1.
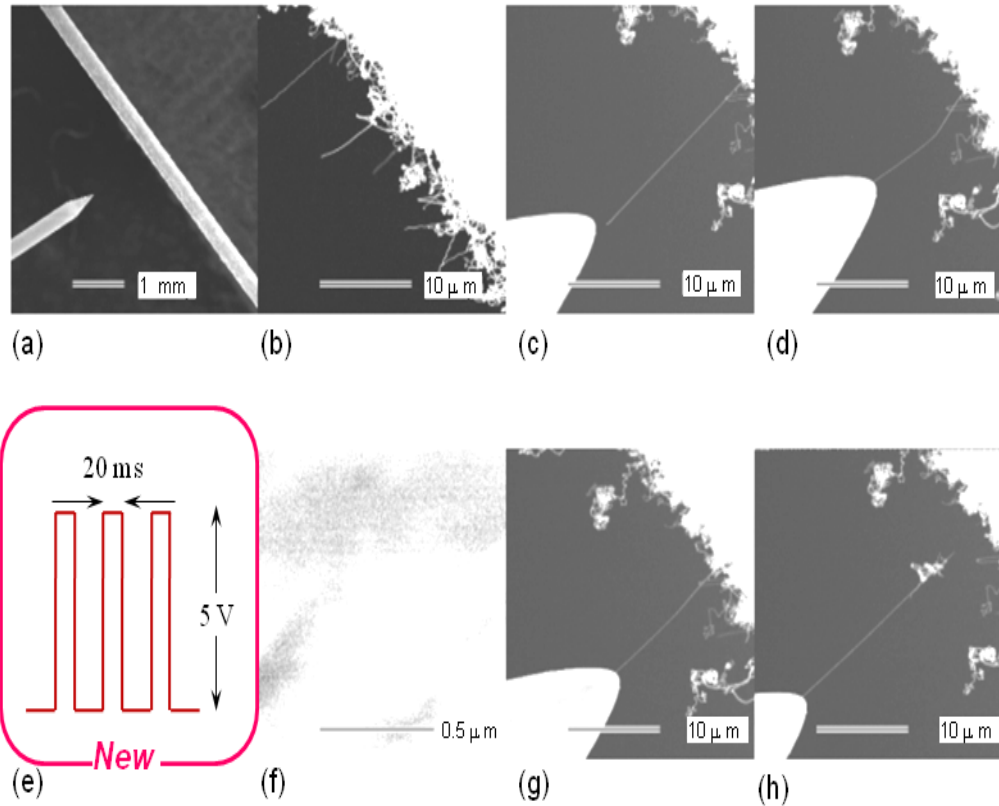
Figure 4.1: (a) The etched W wire is approaching to the W wire with MWCNTs. (b) MWCNTs grown on the substrate W wire surface by CVD method. (c) One selected MWCNT. (d) An initial contact made by a carboneous deposition for 1 minute under high magnification. (e) An intermittent pulse of height 2-5 V and width ~20 msec applied to remove oxide layers. (f) Main welding processes applied for more than 10 mins. (g) Pulling the welded MWCNT. (h) The MWCNT pulled out from the original growth surface after welding.

The left side etched W wire is fixed to our homebuilt 3D coarse-approach stage. It is very important to clean the wire surface chemically before the SEM installation. We used HF chemicals to remove surface oxide layers as much as possible. On the right side the W wire with the CNTs as grown is attached to a 0.75 inch long scanner tubing (0.25" O.D. and 0.02" W.T.). By using the coarse-approach system we can force a mechanical

34

contact between the CNT and the etched W wire. Then we increase the magnification of the SEM to do the routine carboneous deposition welding. It becomes crucial to maintain the magnification of the contact point to at least 85,000 times with an accelerating voltage of 15 kV. Meanwhile we keep applying a fixed bias voltage at a few mV to the CNT and monitoring the current flow by use of an electrometer (Keithley 617). The I-V curve data in this work are all obtained by NI DAQ card and our LabVIEW program. After 1 to 2 minutes of welding for the preliminary fixing, we apply a series of voltage pulses in the range of 2 to 5 V for a short time period in the range of 10 msec to 500 msec under high magnification. Meanwhile, we try to keep a careful examination of the contact. The contact point may go away easily from the screen (the target sight area) because of thermal drift. We do repeat the procedure of Figure 4.1 (e) until the current flow is observed to reach a saturation plateau as shown in Figure 4.2. The stepwise rise of the current flow in 6 steps right after the application of intermittent pulses is an indication of the electrical contact improving in steps due to Joule heating removal of the oxide layers by the application of the voltage pulses. The current jumps with various step sizes, associated with the accumulating removals of the mingled oxide layers in a series of voltage input pulses applied, are also marking the respective times of the succeeding pulse applications in the series. We note that the I-V curves here are monitored at a fixed low bias of a few mV, and the intermittent pulses of 50 to 500 msec width are applied at 5 V. The corresponding currents are in the ranges of a few nano-amperes (nA) and few tens of micro-amperes (μA), respectively. While applying the pulses, the data acquisition was intentionally ceased. Otherwise we cannot examine the nA range current flow at the 4 mV bias.

We may shorten the current saturation time by increasing the SEM magnification, indicating higher e-beam current density contribution to the welding spot. Most of the

observation times, however, the serial application of 5V pulse was more than enough to give a partial removal of the oxide layers in steps to reduce the contact resistance and reach the ultimate saturation limit of the current flow in a few steps as can be seen from Figure 4.2. On the average it takes about 10 minutes at the 120,000x magnification. This means the possibility of making the good contacts several times in a day, which used to be only a few chances during the whole one week with previous methods.

Besides this method based on the observation of the current saturation plateau, we want to introduce another empirical scheme for checking the electrical quality of a junction conveniently. In this second method we apply a small voltage of 0.1 mV in either positive or negative polarity and watch the current. In the first stage of welding, the current flow undergoes fast fluctuations because the electrons emitted from the electron-gun can be accelerated in either direction by the capacitive charging state of the remaining oxide layers at the contact. At this initial time the transient current flow is mainly controlled by the electron-gun emissions and not yet by the small bias application. The current can thus show a wild fluctuation (-1 to +1 nA range) by flowing either to the CNT side or to the etched W wire side if there remains any oxide layer with capacitive charging effects in the appropriate time constant. After completely removing the oxide layers, however, there should be no such fluctuations at all. The steady state current even at this small bias becomes very stable either with or without the e-beam emission, which means the current flow is now controlled by the bias voltage.

The nano-junction contact made in our present work is also mechanically robust. If we attempt to pull out the CNT of our welding contact, it is often pulled out off the original growth surface [see Figure 4.1 (h)] or even breaks at other sites different from the welding site. The contact must be made a perfect metal-to-metal junction between

tungsten and CNT without any intervening oxide layers. What is more important in our work, we want to emphasize that our success rate comes out to be close to 100%.

(a)   85,000x: (830 nm x 830 nm)   (b)   120,000x: (580 nm x 580 nm)
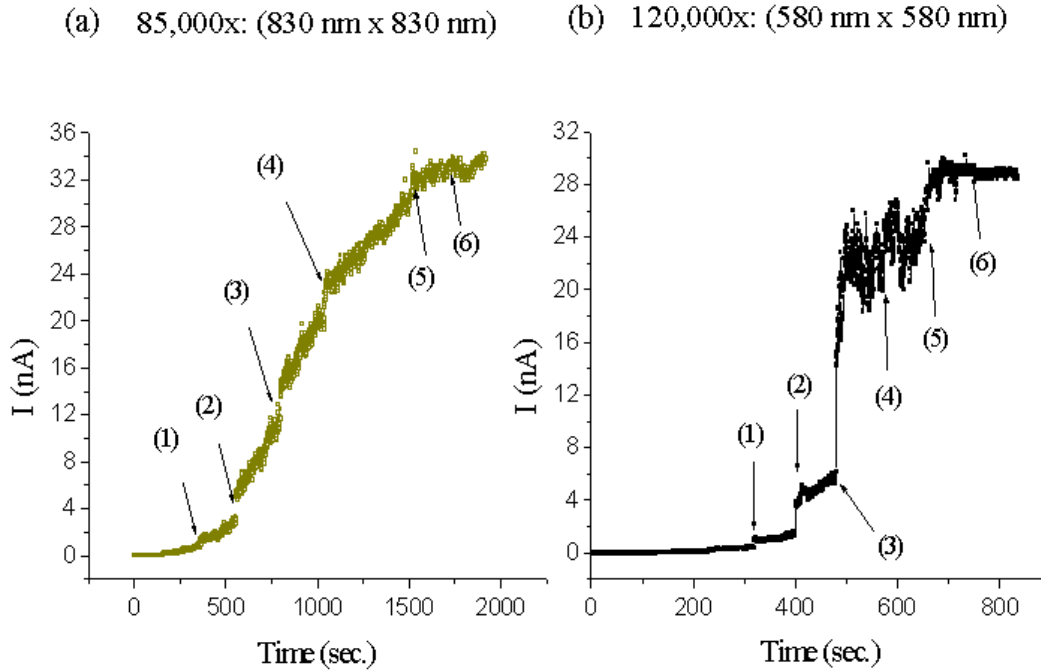
Figure 4.2: I-V saturation curves obtained while welding observations of the CNTs selected for demonstration under 2 different magnifications (a) X 85,000: (sight area of 830 nm x 830 nm) (b) X 120,000: (sight area of 580 nm x 580 nm). Numbers (1) to (6) of the I-V curves represent the respective observation times following the intermittent applications of the serial voltage pulse. Bias of the I-V curve was fixed at the same 4 mV d.c. for both cases of (a) and (b).

The fabrication of the single CNT tip on the Si cantilever was reported [25] to be possible by applying a large voltage (30 V). This high voltage may lead to irreversible changes in the electronic properties of the CNTs. Lu *et al.* have also reported a firm contact between a single CNT and the substrate [26]. They could weld, forming the contact point by using paraffin flux, which may be good for the mechanical property

37

experiments of stress and strain measurements. However, this method may not be adequate for the electronic transport measurements due to possible contamination from the paraffin flux.

4.3 CHARACTERIZATIONS OF THE WELDED TIP

The present method of ours provides another important benefit besides a very stable metallic contact. After forming the contact the CNTs would remain free of any welding-induced qualitative (microscopic) damage. We believe this is due to the very low intermittent input powers from the serial pulses employed, which can be easily checked *in situ* from the I-V characteristics measurements inside the SEM.

Figure 4.3 shows a typical I-V curve obtained after the welding, and Figure 4.4 gives a typical Ohmic resistance value in the linear response regime (with the MWCNT of our tip contact). The I-V curves of the CNTs are observed to remain almost unchanged even breaking off by pulling and after making reconnection.

We also tried to make use of the Van der Waals forces to make firm contacts with the CNTs. This method of making contact is well accepted as good enough to observe the tunneling current as described elsewhere [27] for the STM experiments. Most of them, however, failed to sustain the strong and good electrical contact against external applications of various abrupt mechanical forces.

Oxide barrier removed
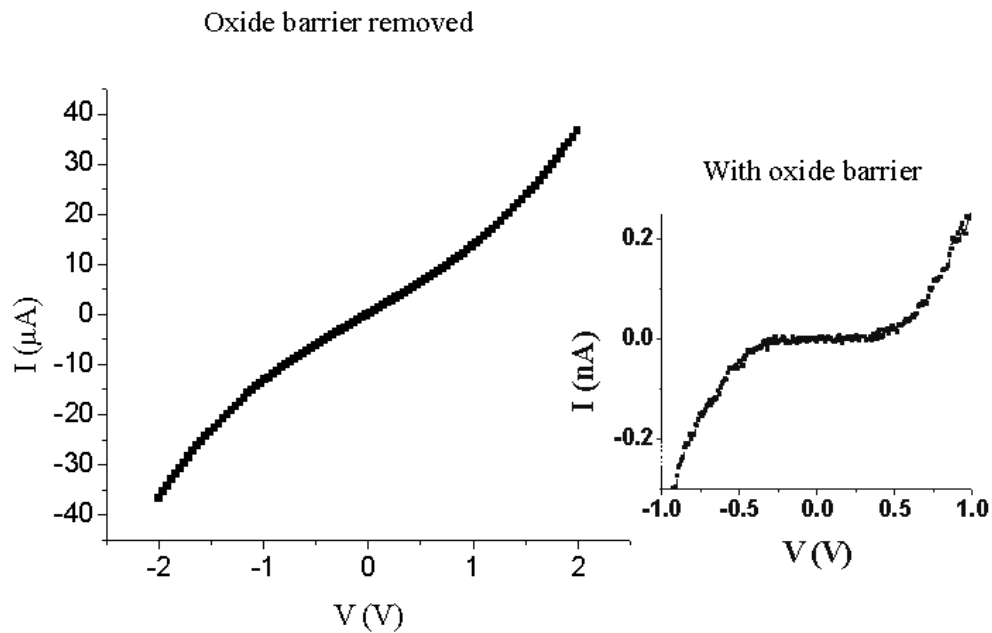
Figure 4.3: Electronic transports in a typical MWCNT. The main frame curve represents a typical I-V characteristics of the MWCNT with our metallic welding contact free of the oxide layers, the inset in the right represents a typical I-V characteristics of the MWCNT with a common oxide layer in the contact, and thus showing a large tunneling gap due to the oxide barrier.
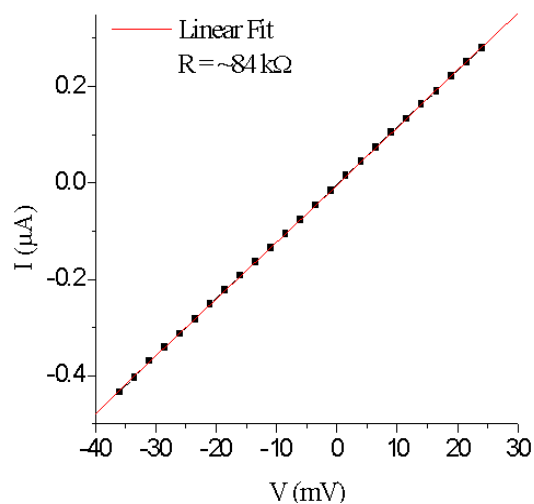
Figure 4.4: Linear fit in the low voltage limit to the I-V characteristics of the MWNT with the contact made by our serial welding method.

39

4.4 SUMMARY

In this chapter we have demonstrated a very simple and easy way to make a reliable clean contact between CNTs and W wires. Figure 4.5 depicts some illustrative CNTs making contact with the etched tungsten (W) wire in varying lengths obtained by this method. We do not need such high temperatures or controlled gas supplies to reduce all the extra contact resistance as in previous studies [28]. This simplest welding method has not been reported yet elsewhere although it may seem to be as trivial as a Columbus egg. Before finding out this simplest method we could make it possible to obtain an unidentified CNT contact only a couple of times in a week. However, with this simple reliable welding method applied, the success rate is so highly improved that we may now make a few contacts in a day. The contact seems to be strong so that it may well sustain many severe mechanical tests involving a hard pulling such as Young's modulus test, etc. Also it can now be used to supply the ideal SPM nano-tips [29] because of the clean metallic junctions obtained at high yields. From the I-V curve measurements *in situ*, we could also confirm that the present method of making welding contacts should keep the welded CNTs intact with their original characteristics.
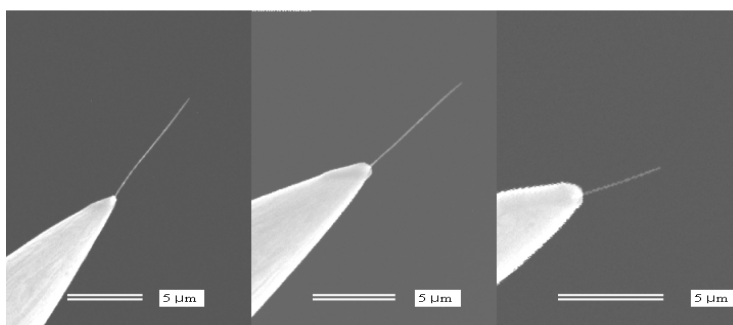
Figure 4.5: Fabricated CNT-W tip contacts in various lengths.

Chapter 5

Transport Measurements in MWCNTs with Bending Deformation

5.1 INTRODUCTION

CNTs have drawn a great attention because of their exotic electronic properties and promising prospects for practical NT applications. The electronic properties can be modified easily by tuning the band structures of CNTs with mechanical deformations because the energy bands of the CNTs are well known to depend on structural changes with respect to chiral vectors of the CNTs, mirror symmetries, nanotube diameters, and thus band gap engineering becomes possible with structural deformations such as bending, stretching, twisting, etc.

While there have been many experimental works reported on the electronic transports in CNTs, most studies are done with the CNTs in contact with a substrate. This constraint leads to concerns about possible electronic interactions of the CNTs with the substrate and further complications due to surface charge trapping. To avoid these complications, our approach is to measure freestanding CNTs, and the transport measurements as a function of a variable strain, which is not possible with the CNTs attached to a substrate.

In this chapter we want to describe our intensive studies on the transport properties with 3 different MWCNTs in variable bending deformations. The first sample, the longest one, has a length of about 9 μm with a gradual bending arc in the middle, the second one with the shortest length of 4 μm, and the third sample is 7.5 μm long with a sharp kink at around the midpoint. We tried for many others but without successful results. We performed the measurements at both room temperature (300 K) and liquid nitrogen temperature (78 K).

5.2 BENDING EFFECT ON ELECTRIC TRANSPORT OF MWCNTS

5.2.1 Continuous Bending at Room Temperature

Figure 5.1 shows SEM images of a CNT in various states of bending. The state of (a) is before making the contact, (b) corresponds to the state after making the point contact with the W wire. The largest bending, in (e), corresponds to a strain level of ~10 % (ΔL = ~900 nm). Bending here is accomplished by a piezoelectric movement of the CNT-attached W-tip (on the right side) equipped in the piezo-tubing toward the fixed W wire (on the left side).

The MWCNT can be seen to have a bending site around the middle. We can also notice, as can be seen from the images, that the left side of the bending is more flexible for further bending in comparison with the right side. That is, although the MWCNT is given a uniform stress the strain distribution is not even. The strain is more concentrated around the bend.

We want to mention also that there appears some stretching deformation accompanied by the unbending as can be seen from Figure 5.1 (h). With a close examination we may convince ourselves of such stretching effect near the bend.
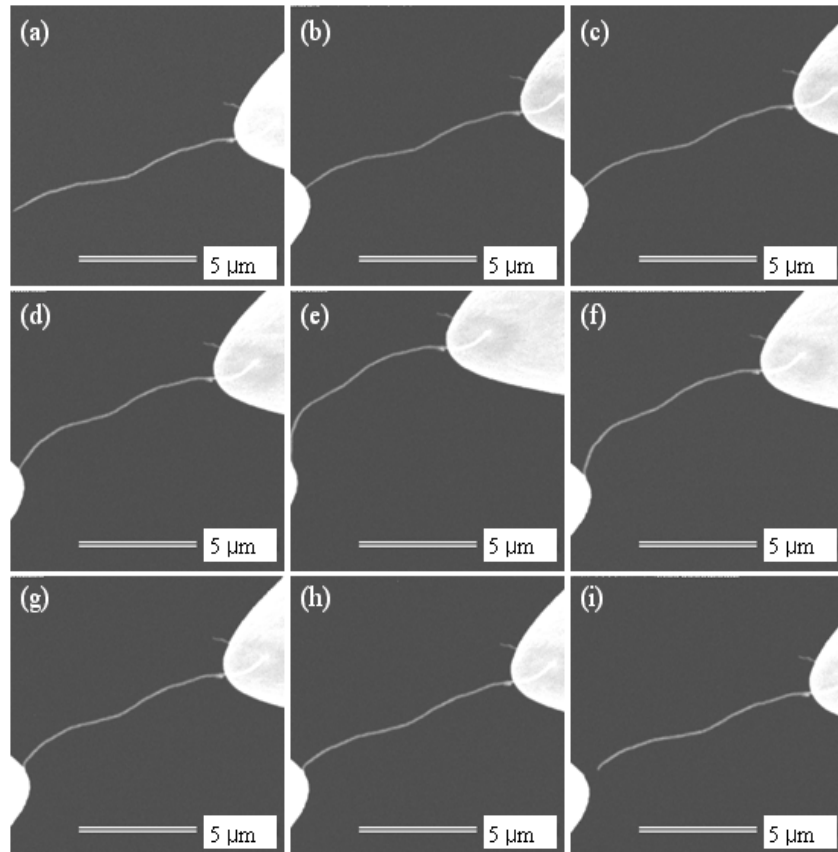
Figure 5.1: SEM images corresponding to different bending states in a MWCNT: (a) a free-standing MWCNT, (b) after making the contact with the W wire (c) $\Delta L = \sim360$ nm, (d) $\Delta L = \sim540$ nm, (e) $\Delta L = \sim900$ nm; (f) to (h) each a residual strain in the reverse cycle (or pulling-out) displacement; (i) back to another free-standing state of the MWCNT. ΔL gives the strain level.

All the experiments reported in this chapter were performed *in situ* inside our home-built probe chamber [Refer to chapter 2 for the details of the LT-HV Probe], where we use the MWCNT tips obtained by metallic bonding between the MWCNT and the W-

tip. The substrate was obtained by gold (Au) deposition on mica with a layer thickness of 120 nm.

Our "continuous bending experiment" means that we are measuring the response function *in situ* with steady state stress applied at various levels to the CNT. As far as we know this kind of experiment with the stress as a continuous control variable has not yet been reported elsewhere.

The room temperature measurements of a current response as a function of the continuous bending variable are shown, at each fixed bias of -15 mV to +25 mV, in Figure 5.2. Also the same room temperature measurements of current in the reverse order of the bias application from +25 mV to -15 mV are shown in Figure 5.3. The x-axis variable, relative position, represents a corresponding relative piezoelectric tubing displacement, which gives in turn either bending (in the pushing-in movement cycle) or unbending (releasing, in the pulling-out movement cycle) deformation to the CNT, depending on whether the tubing displacement pushes in the W-tip towards the substrate or pulls out the W-tip away from the substrate. The piezoelectric element PZT-5H[7] was used in our piezo-tubing. With our piezo-tubing geometry, this system was found to cause a reversible stretching or contraction of ~157 nm in the MWCNT by applying 10 V to the tubing, for example, at room temperature.

We can immediately observe the hysteresis in all the data. This seems to be universal in all the strain-current curve experiments with CNTs. We will come back to address this effect with more discussion and details later.

Fluctuation noises are also noticeable in the measurements at room temperature. However, continuous runs of bending and releasing cycles with the current flowing seem to anneal out some of the fluctuation noise.

---

[7]EBL Products, Inc. EBL#3
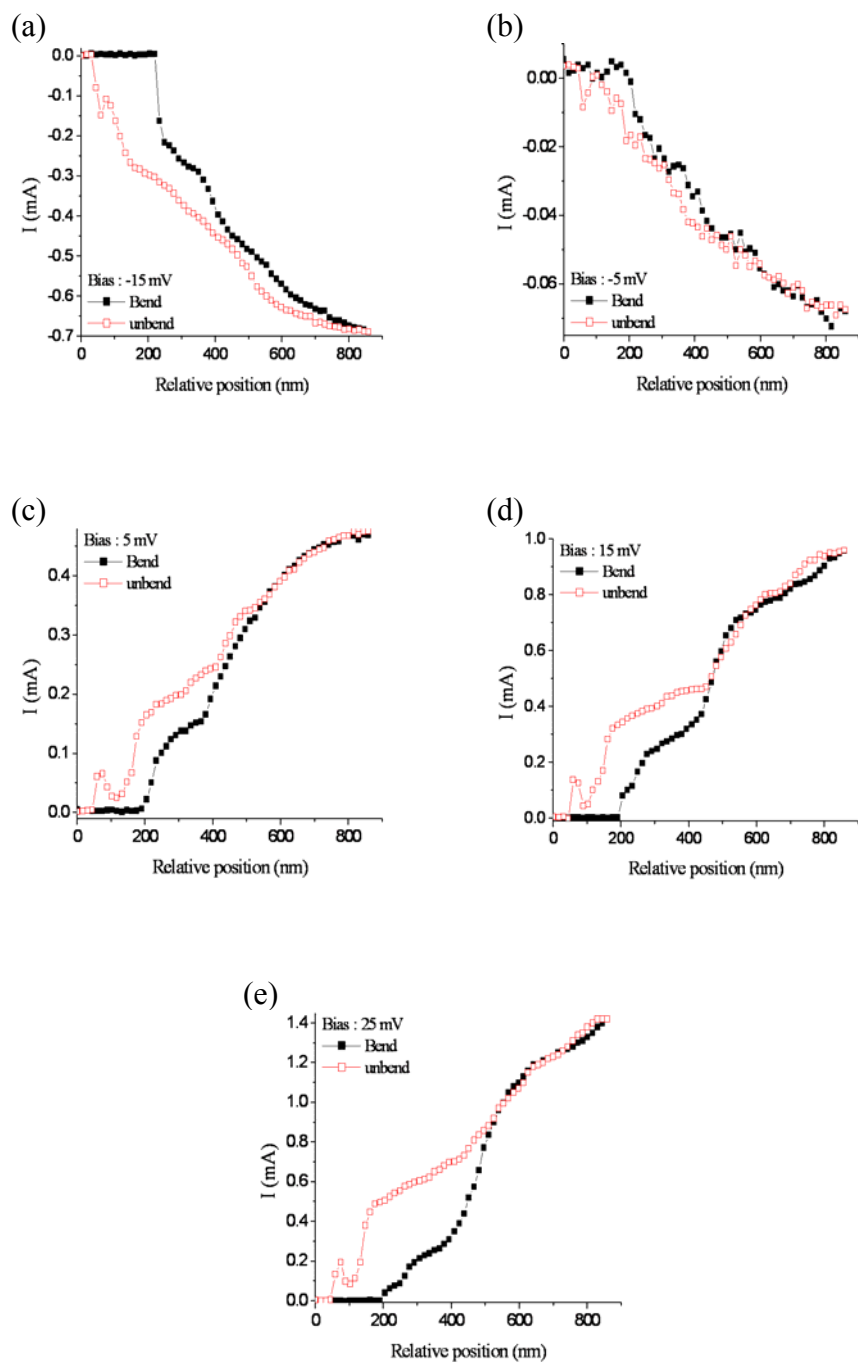
Figure 5.2: I (current) vs. relative displacement measurements at a given bias with the bias application increasing from -15 mV to +25 mV: (a) V = -15 mV, (b) V = -5mV, (c) V = +5 mV, (d) V = +15 mV, (e) V = +25 mV.

45
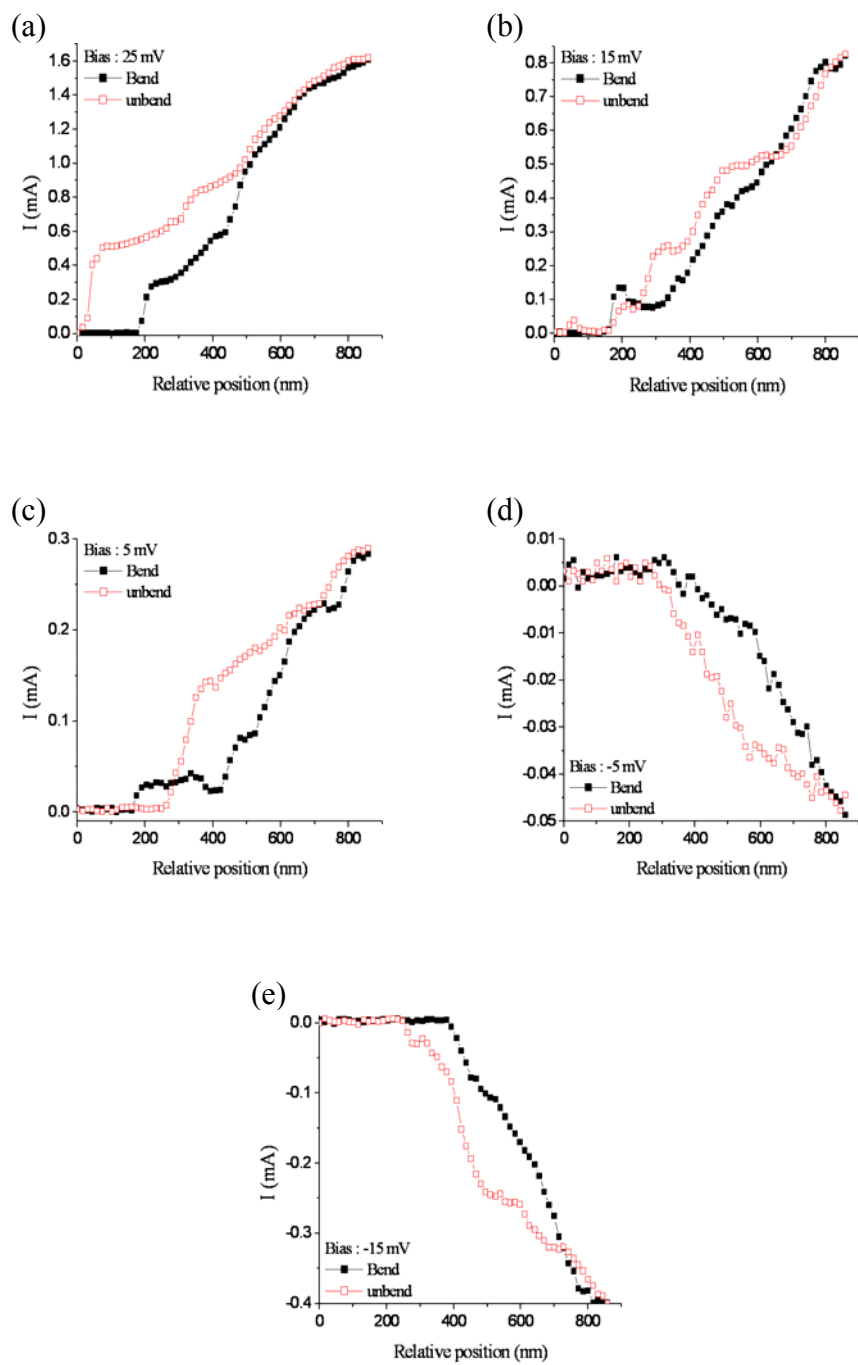
Figure 5.3: I (current) vs. relative displacement measurements in the reverse cycle of the bias application decreasing from +25 mV to -15 mV: with the bias fixed at (a) V = +25 mV, (b) V = +15mV, (c) V = +5 mV, (d) V = -5 mV, and (e) V = -15 mV.

We also note that a small peak appears repeatedly in the releasing (unbending) cycles at around 80 nm of relative position, as can be seen in Figure 5.2, is hardly observable in Figure 5.3 even though the measurements are done with the same CNT and the standard gold substrate. The results of the continuous bending measurement with the CNT, showing the hysteresis loops, may thus involve some nonequilibrium transitions encountering different local valley states depending on their respective thermodynamic pathways between the same initial and final states. This non-equilibrium local effect in a uniform steady state bending may be induced by local site pinned defects. These non-equilibrium strains at pinning site defects might be further explored for NT applications by doping or coating. For example, a magnetic ion-doped or inserted CNT may be used to develop an AFM or STM magnetic nano-tip to probe the local distribution of magnetic moments in CMR or GMR systems. These nanoscopic probes of nontrivial distributions of magnetic moments may well be a vital importance to understand the mechanism for the CMR and GMR phenomena.

5.2.2 Continuous Bending at 78 K

Low temperature (78 K) results of measurements continuing from the previous room temperature runs at various fixed values of bias in the range from -55 mV to +45 mV are shown in Figure 5.4. Fluctuation noises are mostly annealed out here during the cooling cycle run from room temperature to 78 K.

The hysteresis loops are observed to remain, but the thermal noise fluctuations are greatly reduced at this low temperature (78 K). For the piezoelectric voltage application of 10 V, the MWCNT is found to yield a stretching or contraction displacement of ~55 nm at liquid nitrogen temperature with the same PZT-5H piezoelectric scanner tubing.
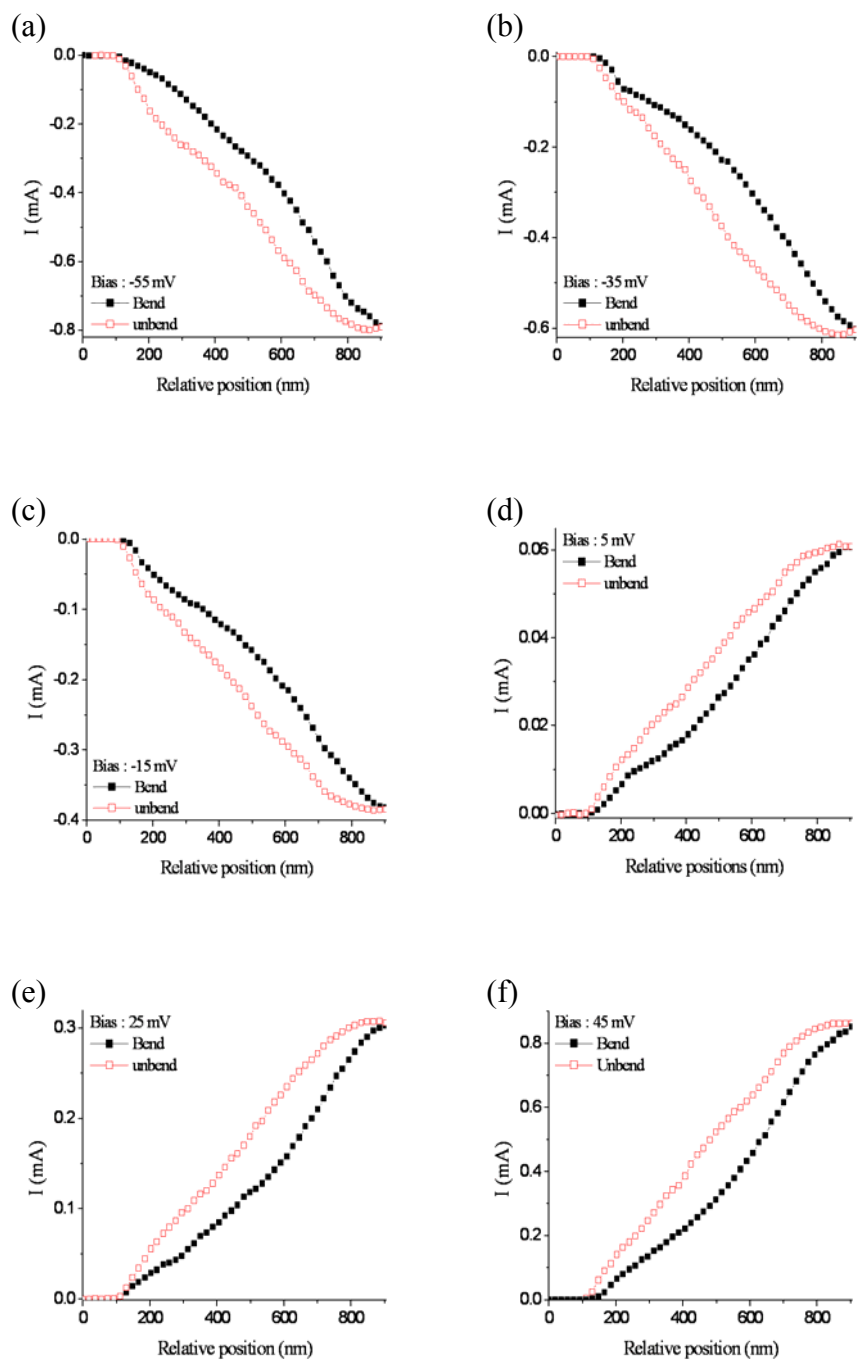
Figure 5.4: I (current) vs. relative displacement measurements at 78 K with different bias applications fixed at, (a) V = -55 mV, (b) V = -35mV, (c) V = -15 mV, (d) V = +5 mV, (e) V = + 25 mV, and (f) V = +45 mV.

48

We can also observe a clear distinction between the initial fast response region and the final equilibrium slow response region. This observation was further studied with another MWCNT to go bending further beyond the linear response regime. The nanotube for further experimental works was selected to be shorter and straight, assuming fewer defects in the more straight CNTs [30].
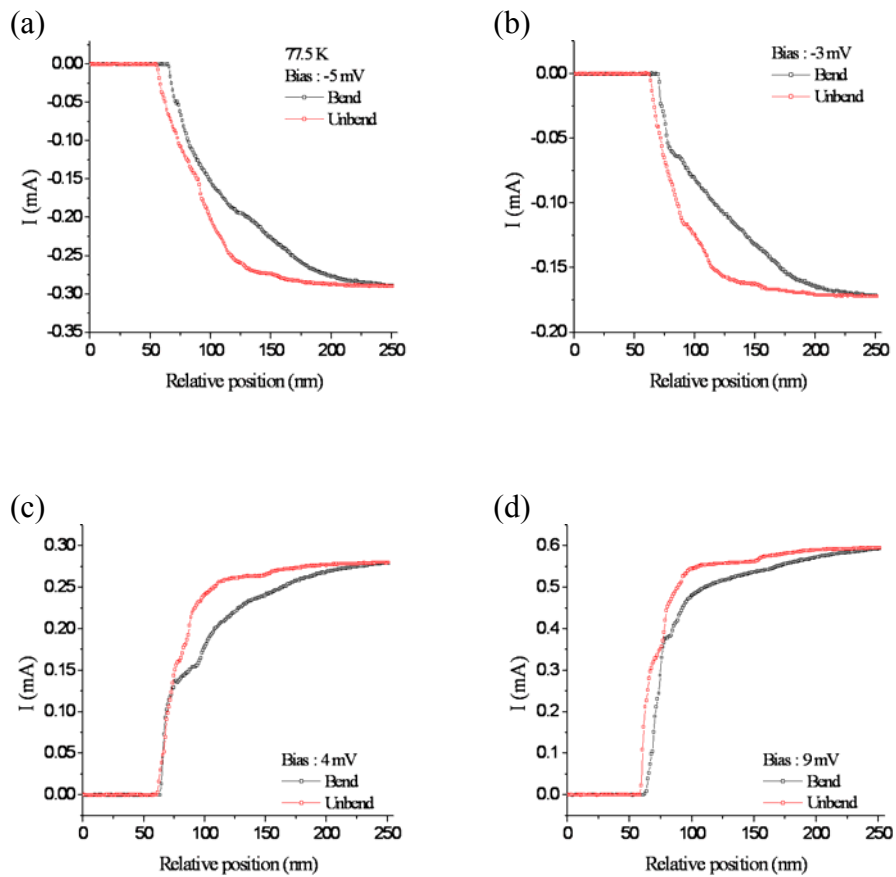
Figure 5.5: I vs. relative displacement measurements at 78 K with the straight 4μm MWCNT at a fixed bias varying from (a) V = -5 mV, (b) V = -3 mV, (c) V = +4 mV to (d) V = +9 mV.

The low temperature (78 K) measurements of I (current) vs. relative displacement for the MWCNT (4 μm length) at fixed values of bias in the range from -5 mV to +9 mV are shown in Figure 5.5. In the first two running cycles of Figure. 5.5 we can clearly observe that there is an initial abrupt response to the bending displacement as given by the fast decreasing changes in current, followed by a second stage of a slow relaxation to the final equilibrium.

The same low temperature (78 K) measurements of I (current) vs. relative displacement curve at a fixed bias (+4 mV) obtained with the 4 μm CNT at two different scanning rates are shown in Figure 5.6. A hysteresis loop between bending cycle and releasing cycle can be more clearly detected. The previous data taken at the 4 mV bias required 200s for the whole loop period (100s for the bending displacement cycle and another 100s for the releasing cycle-Figure 5.5 (b)), whereas in the present case of Figure 5.6 the hysteresis curve in (a) took a data acquisition time of 320s with the relative displacement position up to 450 nm and the one in (b) took 1200s with the same scanning range as of Figure 5.5.

Furthermore, the one in Figure 5.6 (b) can be seen to show the same final bending state with the same relative displacement by ~220 nm, that is, (final position) – (initial position) $= \Delta L = 150$ nm as in the runs with the scanning time of 200 s in Figure 5.5. For all those MWCNTs, the equilibrium properties such as the final equilibrium bending strain would remain independent of the scanning rate or the waiting time as long as they exceed the relevant relaxation time, but the nonequilibrium runs such as the hysteresis loop measurements can be seen to be dependent on the scanning rate.
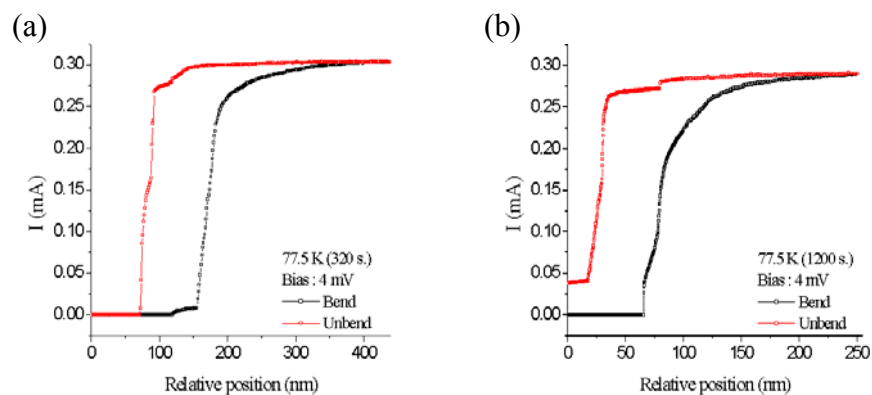
Figure 5.6: I (current) vs. relative position measurements at 4 mV at 77.5 K for the 4μm MWCNT: (a) hysteresis curve obtained in the scanning time of 320s from the CNT with extended deformation [compare with Figure 5.5 (c)], (b) hysteresis curve obtained in the scanning time of 1,200s (slower deformation) [compare with Figure 5.5 (c)].

5.2.3 Summary

We have accomplished a successful experimental system for probing the continuous bending effect on the electronic transport behaviors in MWCNTs, where the CNT can yield to a variable bending distortion with a simple control of voltage applied to the piezo-tubing. I (current) vs. relative position (bending displacement) curves depict both abrupt transitional changes and slow relaxational changes of current with increasing or decreasing bending deformation. Hysteresis loops are formed between the bending and releasing cycles. The hysteresis loop can be seen to have a larger area at slower scanning or with increasing the bending strain level. It seems that there may be a few meta-stable states associated with bending deformations. Both the deep local valleys of long time trapping and shallow local valleys of faster relaxations seem to be encountered within the transitions to new equilibrium states of various strain levels. As the bending deformation cycles are repeated the fluctuation noise is observed to decrease. It may be

51

partly ascribed to thermal annealing of various defects responsible for the meta-stable state valleys by Joule's heating caused by current flows in the repeating runs. Beyond 5 to 10% bending strain, the current flow was observed to be saturated. Beyond this threshold level of strains the uniform continuum strain associated more with the symmetry breaking effect may not be enough to bring about further changes in the energy band structures relevant to the electronic transports but may require a localized strong perturbation possible only by microscopic changes.

5.3 ELECTRICAL TRANSPORT IN BENT MWCNTS

5.3.1 I-V curves of bent MWCNTs at various strain levels at room temperature

Current (I) – Voltage (V) curves of the bent CNTs measured in the linear response regime at room temperature with 4 μm-long CNTs under various bending strains are shown in Figure 5.7. The bending strain in a bent CNT can be calculated with respect to the reference state. The reference state, assigned to a specific value of the relative position (R.P.), is chosen as the state of crossover from the zero current flow to a nonzero current flow. From the reference state chosen at a R.P. reading 86 (refer to captions and insets in Figure 5.7), a bent state of the R.P. 114, for example, gives a difference in the relative displacement ΔL of 114 - 86 = 28 so that the effective strain level ($\Delta L / L_0$) in the state of 114 can be evaluated from the above bending displacement of ~28 nm, where L_0 is the initial length. Figure 5.7 (a) corresponds to the measurements with the bent MWCNTs of various bending strain levels controlled by the scanning electric field applied to the piezoelectric tubing, whereas the results of Figure 5.7 (b) represent the

52

corresponding measurements with the bent MWCNTs of various residual strains after each releasing step by withdrawing the piezoelectric-tubing. Here we can also see the saturation behavior.
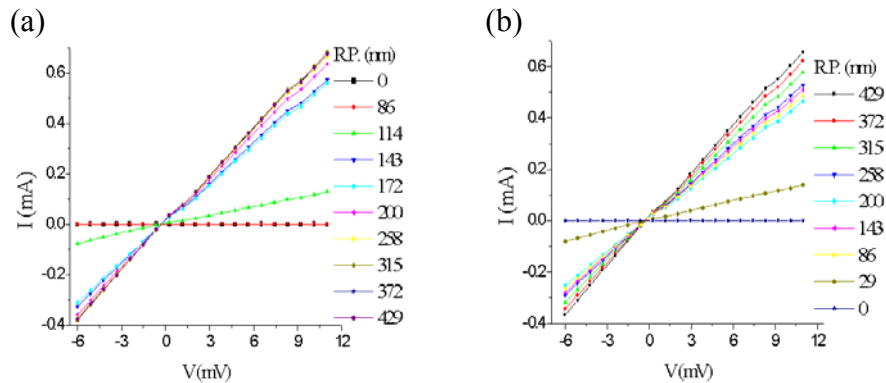
Figure 5.7: Small field electrical transport behaviors of the bent MWCNTs in a series of bending strain levels observed at 300 K. (a) in the order of increasing strain levels with bending displacement cycle, (b) in the order of decreasing strain levels with releasing cycles.

5.3.2 I-V curves of the bent MWCNTs at Low Temperature

Low temperature I (current) - V (bias) curves are depicted in Figure 5.8 for the 4 μm CNT of different strain levels. The low temperature (78 K) conductance dependence on the bias at various bending strain levels in the releasing (unbending) states is also shown in Figure 5.8 (c), where we can locate a minimum dip at zero bias, which was not obvious from the direct I-V curves of Figure 5.7 and Figures 5.8 (a), (b).
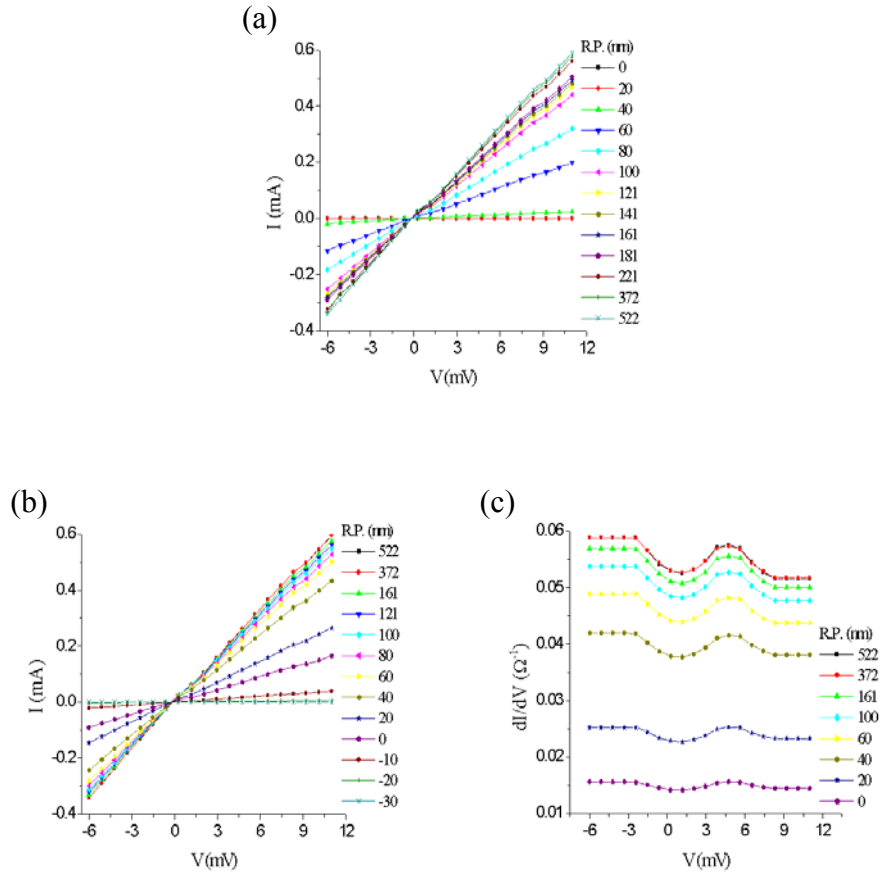
Figure 5.8: Low field characteristics of electrical transport in the bent MWCNT observed at 78 K: (a) in the bending states, with the measurement in increasing order of the strain level, (b) in the releasing states, with the measurement in decreasing order of the strain level, (c) conductance curves obtained by a few selections from (b).

5.3.3 Summary

We have obtained electronic transport characteristics of the I (current)-V (bias) curves for the 4 μm MWCNT at various bending strain levels. Room temperature resistance is decreased by about 10 - 15% in comparison with the low temperature one at 78 K in qualitative agreement with the previous works [31, 32]. It seems, as from the I-V

curves of Figures 5.7 and 5.8, that our MWCNTs selected for the experimental measurements may thus have metallic properties. However, all conductance curves derived exhibit a definite minimum dip around the zero bias. We may give a speculation that localized weak scattering centers may be formed with the bending strain, and the barrier height of the localization potential may be so low that a small bias may be enough to help overriding the weak localization barriers, increasing the metallic conductance. However, more serious studies of both experimental and theoretical works are required to understand this anomaly of the conductance minimum at zero bias.

5.4 SATURATING BEHAVIOR IN THE BENT MWCNT

5.4.1 I-V curves as a function of bending strain at room temperature

We have also examined the transport properties at several fixed strain levels for the 9 μm MWCNT, which exhibits distinctive inflection near the center. Some unexpected observation was made in the transport measurement, which was reminiscent of the blocking contact behavior associated with semiconductor junctions [5]. The two graphs of (a) and (b) in Figure 5.9 are both obtained with the same bent MWCNT at various fixed strain levels. The (a) series measurements represent the data obtained with the increasing (forward) bias application from -60 mV to +60 mV whereas the (b) series measurements are obtained with the decreasing (backward) bias application from +60 mV to -60 mV. The sequence of the measurements follows the increasing order of the strain level, that is, the data curve in black color in Figure 5.9 (a) corresponds to the first in series of the sequential measurements. This black curve of the relative position (R.P.) 0

constitutes one of the horizontal lines of no current. The second measurement is then presented by the same black curve to be shown in Figure 5.9 (b) where the bias in the reverse cycle is decreased from +60 mV to -60 mV. The third measurement data is then presented in Figure 5.9 (a) as represented by the red curve data of the R.P. 114. Then follows the successive measurement in alternating order of increasing or decreasing bias for the same 9 μm MWCNT at fixed strain levels of various color codes, where each color code is given a respective R.P. number on the right side. In the range of +, -60 mV, we can observe the saturation behavior at the state of the R.P. 229 (green curve), where we can see no further increase in current but remains constant even with the bias increasing beyond the saturation threshold. Even though the two curves of the same R. P. state number in both (a)-series and (b)-series of Figure 5.9 represent the same strain level in the same bent MWCNT, they are measured in different cycles of the bias application. Thus their respective thermodynamic pathways will be different from each other with different memories of metastable states or local minimum valleys responsible for various nonequilibrium relaxations. Indeed, their respective initial or final configurations may be different from each other if the nonequilibrium relaxation persists during the alternating cycles as for the hysteresis curve measurements. With a longer length of the bent MWCNT we may well expect more defects or more local minimum valleys to give a longer relaxation time so that we may study relaxation dynamics in the corresponding wide range of available experimental methods.
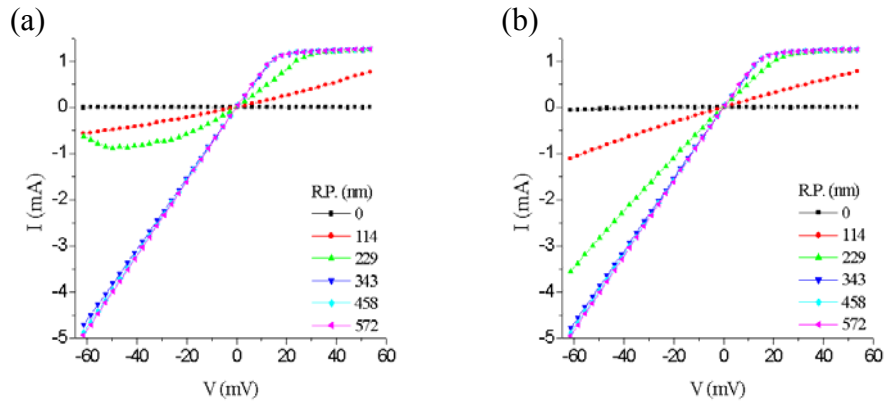
Figure 5.9: Transport properties of the bent MWCNT at various levels of strain at 300 K. Each curve of various color codes represents a different strain level of the bent MWCNT. (a) with the applied bias increasing from –60 mV to +60 mV, (b) with the bias applied decreasing from +60 mV to –60 mV. Note the sequential order of measurements alternate between (a) series and (b) series.

5.4.2 I-V curves of Bent MWCNT at 78 K

Low temperature (78 K) I–V characteristics for the same bent 9 μm long MWCNT under various bending strains are shown in Figure 5.10 (a). Each R.P. number, here also denoted by serial numbers, can be converted to the respective piezoelectric bending strain in the bent MWCNTs. The behaviors of current saturation are observed to start at different points of the bias (saturation onset voltage) with varying strain levels of the bent CNTs. These points of saturation onset voltage are better defined in the conductance (dI/dV) plots of Figure 5.10 (b).

Saturation onset bias voltages are found to best fit an exponentially decreasing function of bending strain as can be seen from Figure 5.10 (c) of the low temperature (78 K) measurements. Bending deformation by a relative displacement of 700 nm can be

57

converted to a 7.8 % strain, a percentile change from the initial equilibrium length. The result of measurements can be best fitted by an exponential curve given by

$$V = A + Be^{-\Delta L / C} \qquad (5.1)$$

where the best fit variables are obtained as A = 36.93, B = 474.64, and C = 150.89.
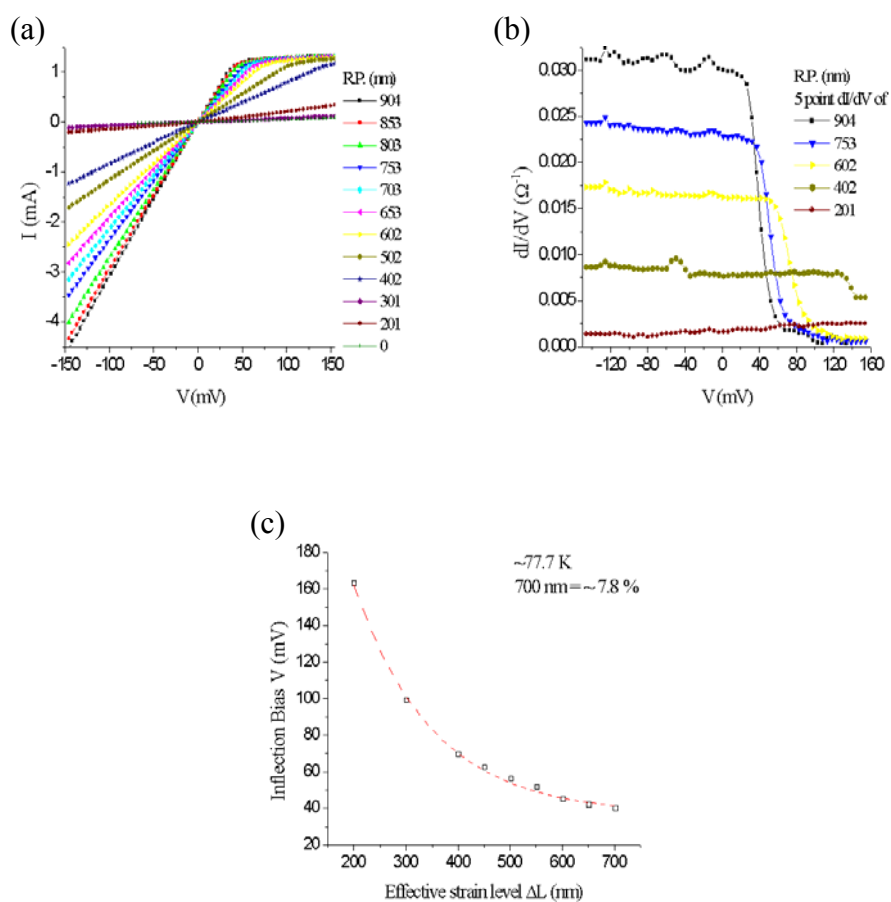
Figure 5.10: Transport measurements of the bent MWCNT in the releasing (unbending) cycle of strains at 78 K. (a) from the unbending (releasing) cycle after the bending deformation. (b) conductance plot as obtained from the data curves of (a), (c) best fit to the saturation onset points as obtained from (a) and (b).

5.4.3 Summary

The onset points of the saturation response with the bent MWCNT may be easily controlled by a small strain change due to the exponential dependence on the strain. This current-saturation onset voltage dependence on the bending strain may be explored for possible applications for switching controls in the NT electronics. In the case of the 9 μm MWCNT the resistance was observed to increase with lowering temperature in the linear response regime up to 30-40%. In combination with our results in previous chapters, we believe the initial abrupt change in the current response may come from the effect by the compression component of the initial bending deformation mostly within the first ~10%. It can affect directly the symmetric honeycomb lattice and the band structure of the MWCNT shells so that the compression may reduce the C-C bond-lengths leading to enhance the overlap interactions in the direction of the current flow and thus hopping contribution from weakly bound electrons to increase in conductance.

5.5 STUDY OF POINTED SHARP KINK

5.5.1 Result and Summary

We want to add a brief comment on our last example studying the electrical transport properties associated with various deformations of the MWCNTs, where we select an intermediate length MWCNT with a sharply pointed kink. The SEM image of the corresponding MWCNT with such a kink deformation is depicted in Figure 5.11. We can also notice that the kink is affected seriously in various forms by continuing changes

in the stress applied. We carried out some routine I - R.P. measurements on this kinked nanotube. As shown in Figure 5.12, the chaotic data observable was never reproducible. With all the 3 data sets obtained from the consecutive running of bending experiments one after another without pause we cannot conclude for anything except that the kink is a very unstable point contact where the energy bands are critical to change with possible contact interactions between various inner shells of the MWCNT at the kink by any kind of infinitesimal perturbations.
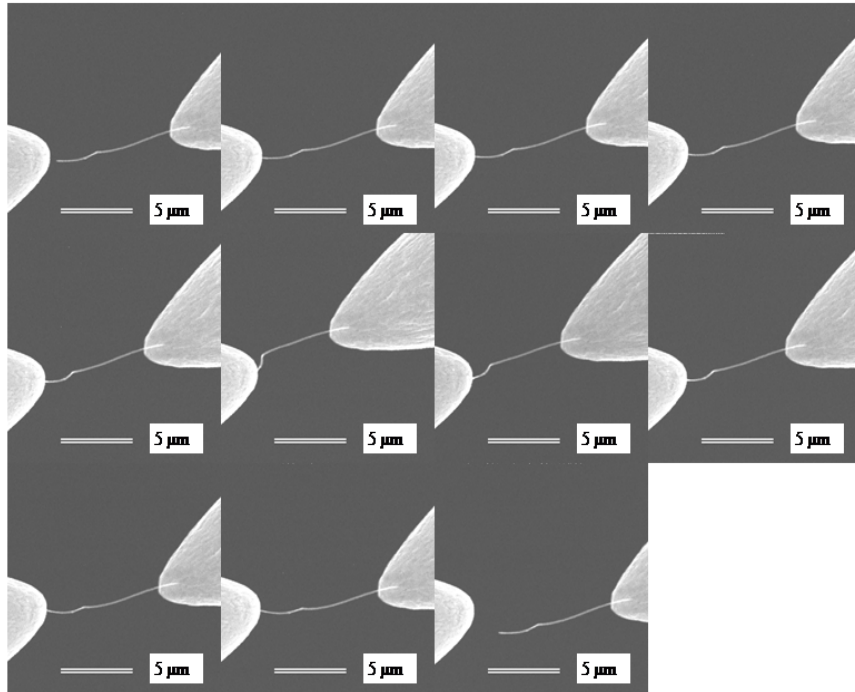
Figure 5.11: SEM images corresponding to each bending state of the kinked MWCNT: (a) a free standing kink-formed MWCNT, (b) after making the contact with the W wire, (c) $\Delta L = \sim 270$ nm, (d) $\Delta L = \sim 360$ nm, (e) $\Delta L = \sim 540$ nm, (f) $\Delta L = \sim 900$ nm; (g) to (j) represents each partially-released state in the respective reverse cycle of continual releasing in steps by pulling out the CNT attached W-tip, (k) back to the free-standing kinked MWCNT. ΔL gives a respective strain level.

(a)

(b)

(c)
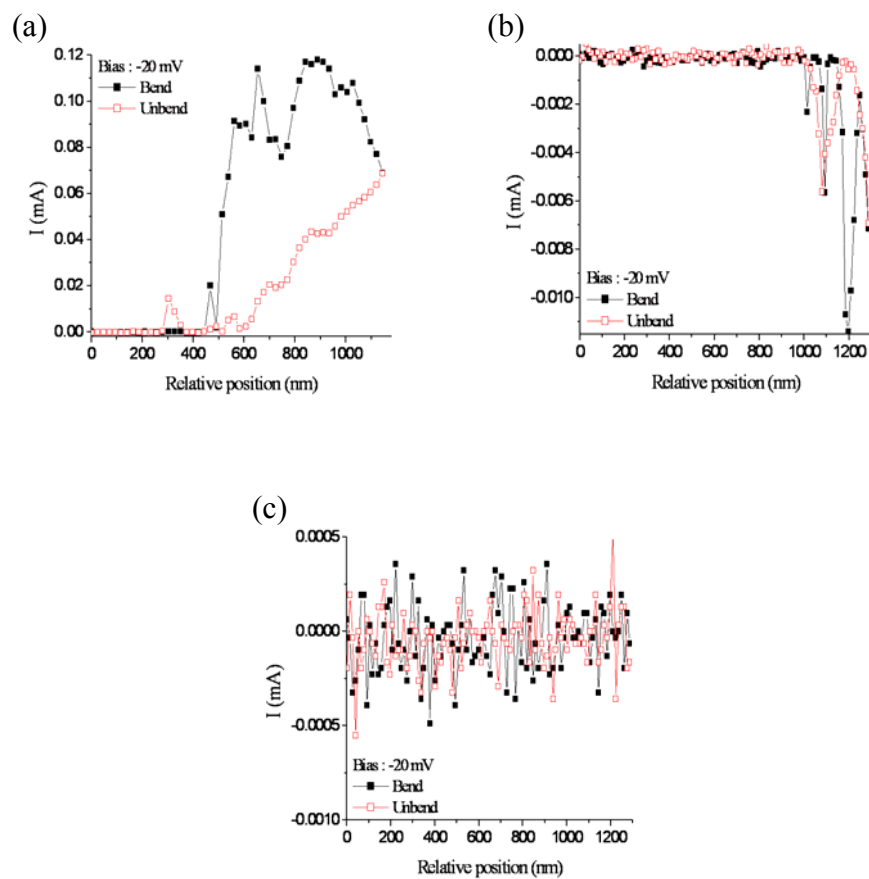
Figure 5.12: Current observations as a function of strain levels obtained in the order of (a), (b), and (c) at room temperature.

5.6 APPENDIX
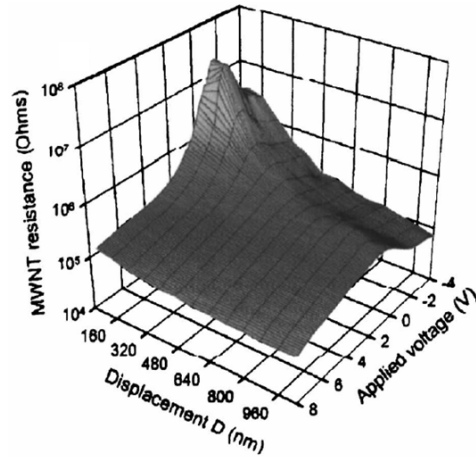
Figure 5.13: Reproduced from V. Semet et al., Appl. Phys. Lett. **87**, 223103 (2005).

V. Semet et al. performed the bending experiment [33] at room temperature. They used n++ doped Si wafer to grow MWCNTs and directly pushed the nanotubes in contact with Pt-Ir ball. Their result is reproduced in Figure 5.13 as obtained for their 5 μm MWCNT. We can also see here the major change coming within the first 10%. This work also supports that our "welding and cutting" method is not affecting the electronic properties intrinsic to the MWCNTs. In other words, we can assume safely that most of changes in resistance of the CNTs subjected to deformations are not coming from the cappings of the MWCNTs.

Chapter 6

Band Gap Change in MWCNTs by Stretching Deformation

6.1 INTRODUCTION

Band-gap engineering of CNTs can make nano-wires of various circuit elements from metals to insulators including semiconductors with varying energy band-gaps. The key factors for band gap control in CNTs are well known to be the chiral vectors defining the wrapping of the graphene sheet (a single atomic layer of crystalline graphite) into hollow cylindrical tubes with a diameter of a few nanometers [3]. Since the energy band gap of a CNT depends also strongly on the diameter of the nanotube [34] we may well attempt the band-gap engineering of CNTs by making use of the stretching deformation which would induce the radial deformation of decreasing the radius.

Although the effects of structural distortions such as stretching, bending, and torsion [35] have been studied theoretically for a while, the electronic structure and the transport behavior of deformed CNTs are not yet fully understood. For realistic applications, the ability to control the electronic energy band gap and thus the electronic transport behavior, via the mechanical deformation of the CNTs, seems to be important.

6.2 EXPERIMENTAL METHODS AND RESULTS

The CNT stretching experiment employing SEM observation was performed as follows. The etched W-tip was brought to a long MWCNT protruding from the surface of a separate W wire to make the welding junction with the MWCNT. After confirming a strong and good bonding contact, the CNT between the W-tip and the W wire can be stretched by using the piezoelectric 3D walker. The current was then measured as a function of the strain level, starting with the highest level in tension so that we may avoid confusions with the contact between the W-tip and the MWCNT. For example, we can remove the uncertainty of whether the current might be caused to decrease by loosening a defective contact due to the pulling force. However, when we begin with the highest level tension, we can convince ourselves that we have the same stable contact throughout the whole the experiment by going through all the pushing and jerking movements using the piezoelectric 3D walker. If we begin the sequence in the reverse order, the contact may fall into the worst stability condition in the final step, that is, Figure 6.1 (a) in the present run, and the most natural interpretation would be that the decrease in current was caused by a loosening of the contact.

Figures 6.1 (a) to (e) show several stages at different strain levels of the MWCNT, corresponding to the respective changes in distance between the moving W-tip and the fixed W wire. I-V curves of the MWCNT are obtained in the order of proceeding from Figure 6.1 (a) representing the least bending, to Figure 6.1 (e) representing the largest bending state. State (a) also corresponds to the maximum stretching. The etched W-tip seen on the left boundary is welded to one end of the MWCNT with the other end rooted (as grown) on the surface of another separate W wire. All the data given below are obtained from different samples of MWCNTs but with the same conditions.
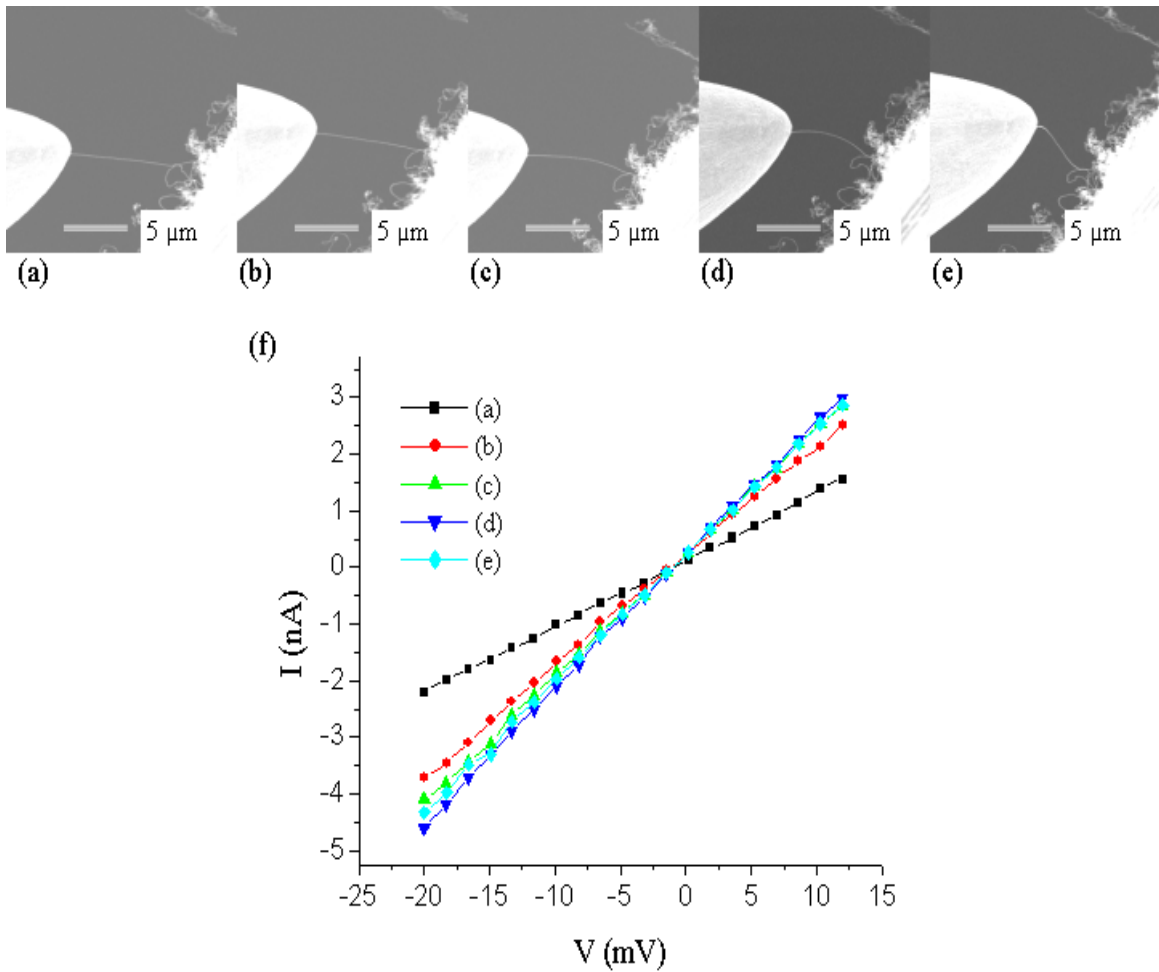
Figure 6.1: (a) to (e) shows the SEM images of the MWCNT subjected to various stretching deformations. (f) I-V characteristic curves, each curve corresponding to the respective stretching in variations from (a) to (e).

Table 6.1, derived from the data set of Figure 6.1 (f), clearly shows that the resistance of the CNT may change abruptly with a very small stretching. The estimations of relative strain are from the photographic (SEM image) data analysis so it may have a large error bar due to 2D projection of imaging.

Figure 6.1	(a)	(b)	(c)	(d)	(e)
R (MΩ)	8.54	5.12	4.55	4.22	4.42
[(Rx-Re)/Rx]x 100 %	48.2	13.7	2.86	-4.74	0
Relative Strain %	47.4	36.8	31.6	13.8	0

Table 6.1: Resistance dependence on the strain. Derived from the data set of Figure 6.1 (f), where the stage (e) of the saturated value was taken as a reference for estimation of the relative changes.

In Figure 6.2, the red curve (made under the compressive stress of the pushing cycle) was obtained after the blue curve (made under the tensile stress of the pulling cycle). The "W-tip to CNT welding contact" was confirmed to remain very stable and rigid before and after each measurement.

The "blue I-V curve" in both Figure 6.2 (c) and Figure 6.2 (d) was obtained in a state of stretching. If we put the blue and the red curves in the same scale drawing, we may not be able to recognize any current flow with the blue curve because of the apparently zero slope.

However, there is a small current flowing as can be seen in the expanded version of the graph shown in Figure 6.2 (d), demonstrating an extremely small but finite current contribution from a metallic channel hidden in the complex networking junction. From Figures 6.2 (c) and (f), however, we observe a gap opening (increasing), as in the case of the stretching deformation.
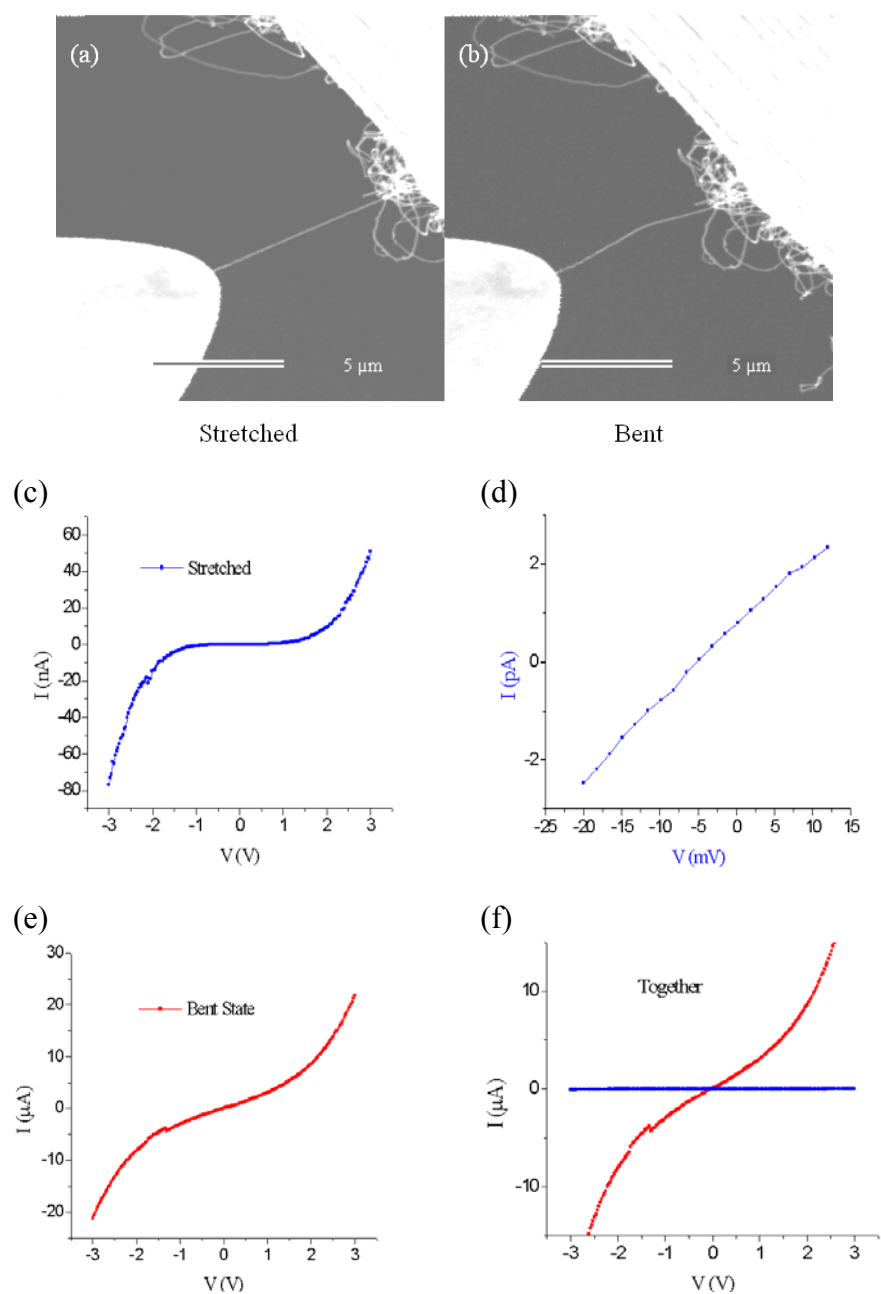
Figure 6.2: (a) SEM image of a stretched CNT, (b) SEM image of a bent CNT, (c) I-V measurement of the MWCNT *in situ* with stretching, (d) I-V curve in the small signal linear response regime (note the bias in the mV range and the current in the pA range), (e) I-V curve taken *in situ* with pushing and thus bending the CNT, (f) The same scale presentation of the two I-V curves for the MWCNT in stretching and bending deformations, corresponding to graph (c) and graph (e), respectively.

6.3 DISCUSSION

When CNTs are stretched along the longitudinal axis of the cylindrical nanotube, itinerant electrons may go localized at the symmetry-breaking sites since the forces by the 3 nearest neighbor atoms are no longer balanced out but tend to point at the sites shown in Figure 6.3, and hence the conductance will accordingly decrease.
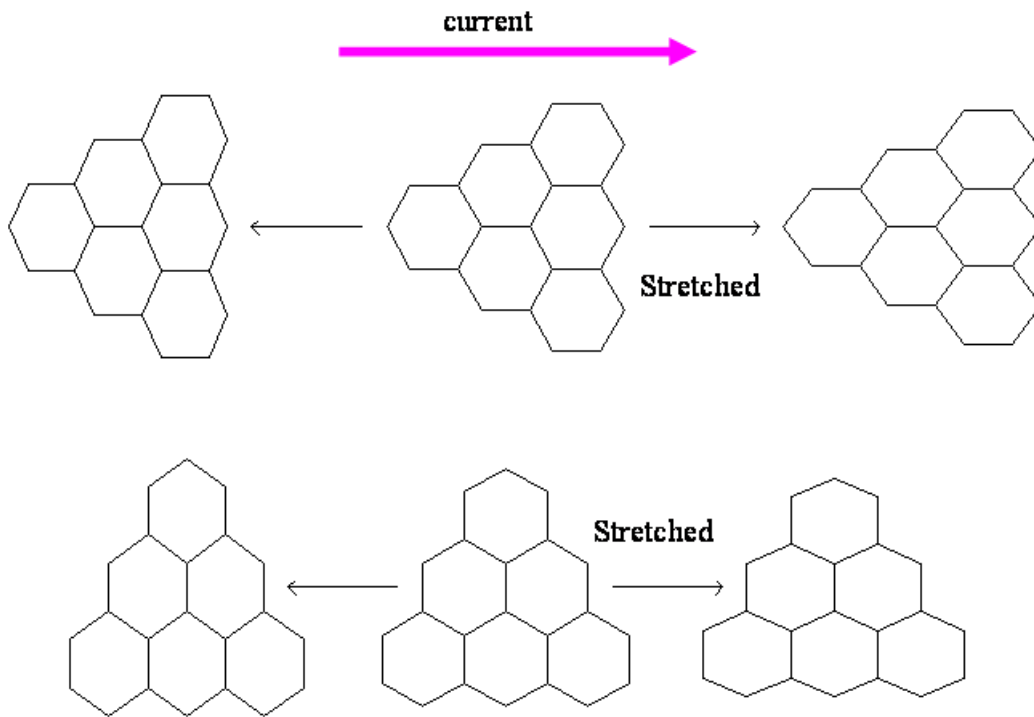
Figure 6.3: The structural deformation accompanied by the stretching deformation. The upper diagram corresponds to the zigzag (metallic) CNT and the lower one to the armchair configuration.

Furthermore, the neighboring atoms will be separated further away in the same direction as the current flow so that the electron wave functions may overlap less in this direction thus reducing the hopping conductivity and decreasing the overall conductance.

Also the distance between the walls of inner tubes can get closer to change by a factor of r^2 slower than the distance between the neighboring atoms in the stretching direction if we assume the CNT volume remains fixed (see Figure 6.4) during the deformation.

The numerical calculations of conductance for some selected chiralities in the stretching deformation are reported to show the conductance decreasing with the stretching [36]. We also carried out many tests of the stretching effects on CNTs and observed the current decreasing without exception. So we may conclude that the current may always be decreasing with stretching deformation.

Figure 6.4: The microscopic structural deformation accompanied by the stretching deformation.

6.4 SUMMARY

We have observed conductance lowering and energy gap changing features with the stretching of CNTs. Figure 6.3 and Figure 6.4 offer a very simple intuitiv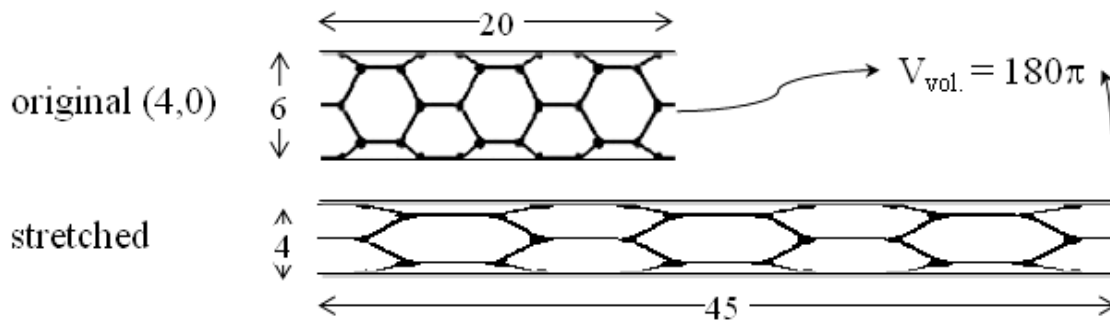e model of ours to explain qualitatively for the electron localization effect. In contrast to the previous work [37], we conjecture from our model above that the conductance may always be decreasing further beyond the level of reductions by a small decrease in radius of the nanotube accompanying the stretching extension. Opposite instances in the previous work [37] may be possible only with other accompanying effects such as local variations in the tube radius at the point of the cantilever-tip contact or changes in the cantilever pressure [38].

Also it should be much easier to tune the band gap with the stretching deformation. The resistance increases drastically with the pulling of the MWCNT due to symmetry-breaking localization effects, even opening an energy gap to alter the electronic transport properties. However, as described in Chapter 5, the bending deformation lowers the resistance up to a certain level of bending ~10%. A combination of these effects may be useful in nano-technology (NT) mechatronics. Since the axial (longitudinal) deformation is hard but the radial (transversal) deformation is easy, the curvature change with the nanotube bending will not give any significant compression. However, all the pulling force in the axial direction would all go directly for stretching the CNT to control the band gap.

Chapter 7

Electrical Transport Properties of the X-junction in MWCNTs

7.1 INTRODUCTION

In the last decade, carbon nanotubes have been emerging as ideal building block elements for nanotechnology. Here we want to investigate electronic transport properties of some modified MWCNTs that may be useful in nano-electronics.

Terrones [39] has shown the formation of molecular junctions with varying geometries formed by joining different pieces of SWCNTs using the e-beam welding technique inside a transmission electron microscope (TEM). The experiment was performed at high temperature of 800 ºC with an e-beam energy of 1.25 MeV. Their TEM results clearly demonstrated that the molecular junctions could be made in various combinations of SWCNTs by using e-beam "nano-welding" at high temperatures.

In the present chapter we want to describe our simple fabrication of the X-junction made with MWCNTs by using the e-beam of energy in 'keV" range at room temperature *in situ* in the SEM. We will also describe our experimental results obtained from the electrical characterization of the X-junction.

7.2 X-JUNCTION WITH CARBON NANOTUBE

7.2.1 Fabrication of an X-junction in a MWCNT

In Figure 7.1 we depict how we made the X-junction with MWCNTs. We first select one MWCNT grown on the W wire surface. The MWCNTs on the W wire are grown by the CVD method as described in chapter 3. For this experiment we select separate MWCNTs. Then we attach the selected MWCNT to the chemically etched and cleaned W-tip. Next we follow all the procedures step by step as described in chapter 4 to obtain a clean and firm metallic contact (Figure 7.1 (a)) between the nanotube and the W-tip. We then pull out the nanotube by applying a negative voltage to the piezoelectric tube supporting the MWCNT as grown on the W wire so that the selected nanotube may be cut at the weakest spot (Figure 7.1 (b)). When the selected CNT is free of defects it becomes difficult to cut. Often the CNT breaks off from the rooting growth point. After making a successful cut in the nanotube into two pieces, the left one (previously welded to the W-tip) is moved to make a mechanical contact to the right one that is rooted in the substrate (Figure 7.1 (c)). The moving part can be moved in the X-Y-Z directions by the 3D walkers, as described in chapter 2. The MWCNT X-junction then can be formed by welding by the e-beam in the SEM at a high magnification of 200,000x. The e-beam energy was 15 keV. The exposure time for welding varies from 1 min to 10 mins. The MWCNT to MWCNT junctions so obtained are found to be strong enough to survive all the pulling tests (Figure 7.1 (d)).

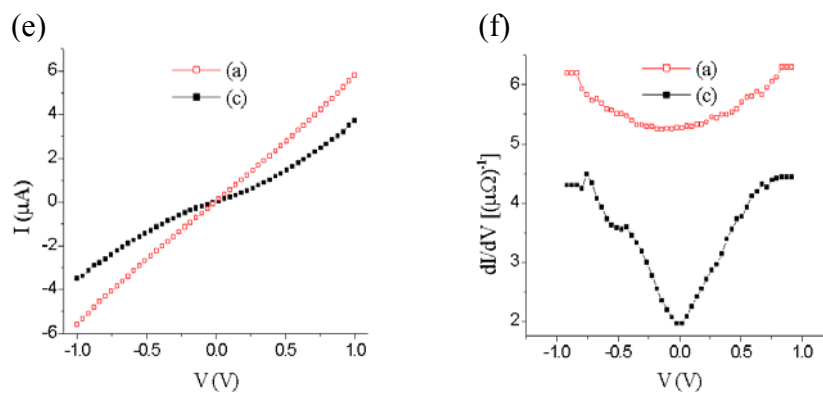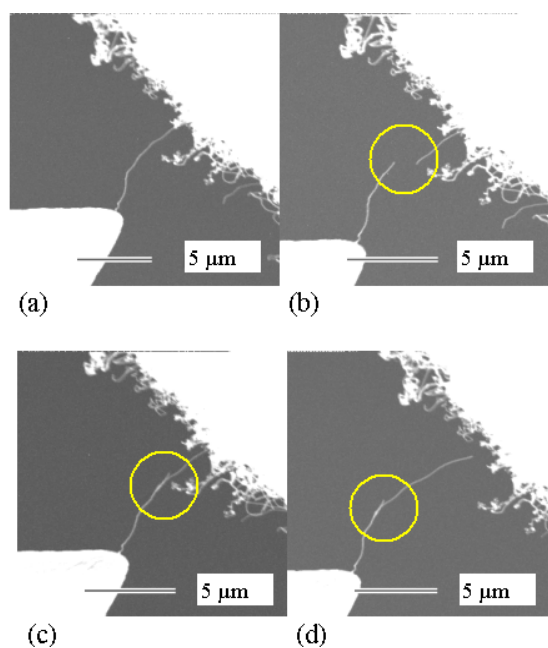Figure 7.1: (a) After the e-beam welding of a MWCNT. (b) By pulling out we can cut the weakest point of the MWCNT. (c) The two separate pieces of the MWCNT were rejoined by using the e-beam. (d) The jointed MWCNT was pulled out by use of the 3D piezo-walker. (e) The red curve was obtained before cutting (a) and the black one was obtained in the state of (c). (f) dI/dV obtained from the data in (e).

7.2.2 Electrical Transport Characteristics of the X-junctions in the MWNTs

If we make the X-junctions of the CNTs following the earlier work [39], we need 3 steps or more to measure the electrical transport characteristics of the junctions. That is, the transport properties for each of the two SWCNTs should be characterized in advance to find the unique molecular junction characteristics derived from the two. However, with our experimental setup we need only 2 steps to solve the same problem since we have the I-V curves obtained already in the previous step as shown in Figure 7.1(a), that is, before the cutting. The X-junction can provide various conduction channels between various shell tubes of the MWCNTs (Figure 7.2). Most samples of the MWCNTs available in the experimental works are composed of both metallic and semiconducting CNTs. Hence we may also expect to have metal-insulator junctions, quantum dots, etc. with the formation of the X-junction.
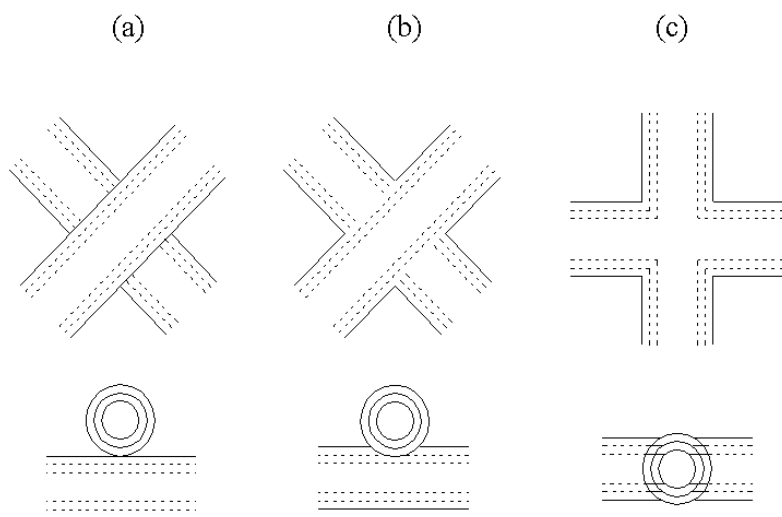

Figure 7.2: A schematic drawing of the X-junctions in the MWCNT (a) to (c) shows formation of X-junction (cross junction).

74

We measured the I-V curves in Figure 7.1 (a) before the cutting and then obtained the I-V curves in Figure 7.1 (c) after the formation of the X-junction so that we may compare between the two. The I-V curves so obtained are both shown in Figure 7.1 (e). Figure 7.1 (f) is the conductance dependence on bias voltage as derived from these I-V curves. If we compare the two I-V curves in close examination, the electrical transport characteristics of the MWNT seem to be transformed from ohmic linear response behavior to non-ohmic nonlinear response behavior. It is very interesting, however, to see from Figure 7.1 (f) that the conductance minimum does appear around the same zero bias for both in symmetric response with respect to the positive and the negative bias. It seems therefore that there may be no sudden barriers formed with the X-junction or the major current flow still resides in the outermost tube. However, there seems to be more room to reduce the resistance further by modifications in the fabrication procedures such as a variation in soldering time.

Another example of the contact junction may be selected as in the following to depict an outline of the time series developments for the "nano-welding" and its corresponding stability of the electrical contact. The junction made in the example has a T-joint shape rather than the X shape, as can be seen from Figure 7.3 (a). We examined the current fluctuations *in situ* at a low bias to determine when the surface welding contact is stabilized. The magnification in the operation was normally chosen above 170,000x with an e-beam electron energy of 15 keV. The SEM field of view covers a small area at this magnification and the junction site may go off easily, disappearing from the screen. This initial settling of the focus, as well as the contact making instability, may lead to the large fluctuation noise observed in Figure 7.3 (b). One can stop the welding when the current saturation is observed. In other words, the contact resistance can be seen to stabilize with the completion of welding throughout the whole contact surface.
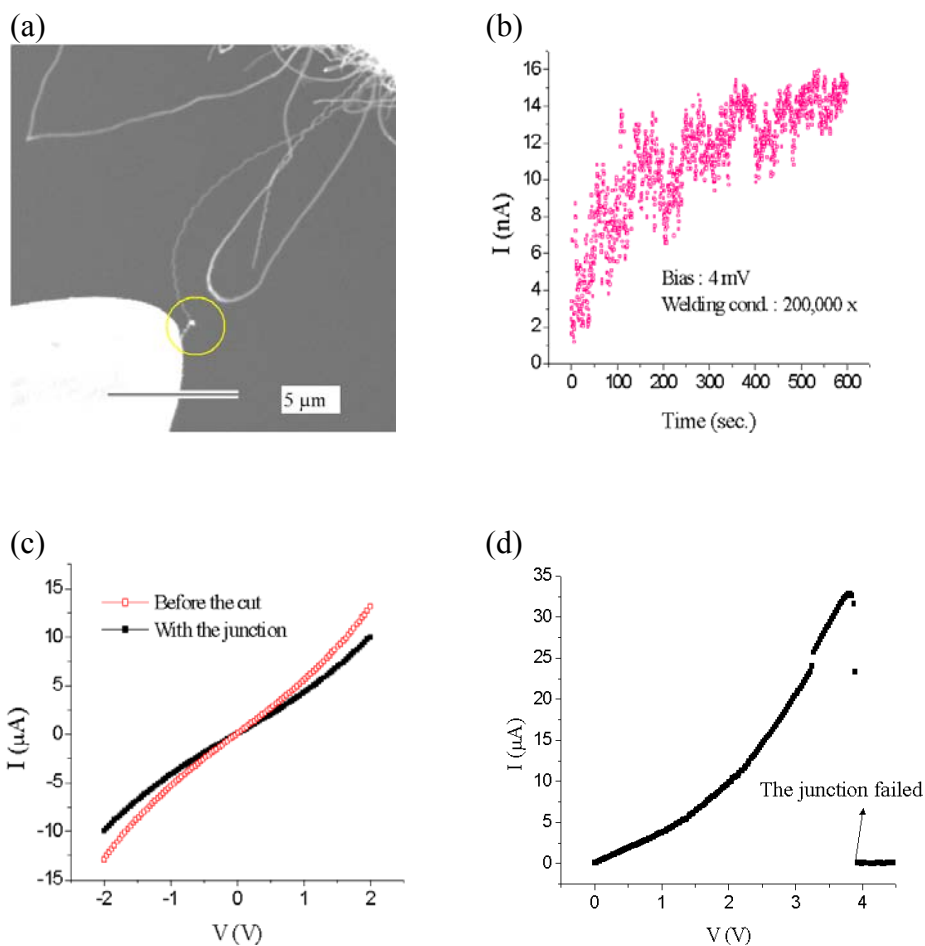
Figure 7.3: (a) Another example of a contact junction with the MWCNT, (b) Monitoring the current fluctuations at small bias while making the junction, (c) Characteristic I-V curves of the MWCNT junction, (d) the T-junction was tested for its failure by increasing the bias above the threshold.

Our observations are compatible with a previous work on the relation between the welding exposure time and the contact resistance [40]. Figure 7.3 (c) shows the electrical transport characteristics for the nanotube junction. After making the CNT-CNT junction, we made an electrical breakdown test for the junction to find out the working limit by extension to higher voltage and current, as depicted in Figure 7.3 (d). This T-junction was observed to remain intact in the range of applied voltage up to ~3.8 V, but to fail when

flowing a large current above the threshold of ~34 µA at ~3.8 V. These values may not be universal but can be an order of magnitude indication for forming surface-welding junctions with CNTs.

The last example of junction formation with MWCNTs shows an unusual result in the I-V curves. The junction made for the test is shown in Figure 7.4 (b) and the respective I-V curves are shown in Figure 7.4 (d). The current was found to increase after forming the junction, in contrast with the previous examples where the junction formation made the current decrease. This observation may be explained by assuming that the X-junction can increase the connection channels between the outermost and the inner shells containing metallic CNTs.

Radial distortion (changes in radius) may also occur with the formation of the X-junctions. Radial distortion can bring about a significant change in the energy band structure depending on the chirality of the starting states [41, 42]. With the armchair structure the energy gap increases with increasing radial deformation while, with the zigzag structure, the gap starts to increase in the beginning of a small change, but with further distortion (decreasing the radius) the gap may be reduced and close because of the ultimate overlap interactions of σ-π orbital hybridization.

Another explanation for the decreasing resistance is we assume that the break happened at a major defect which had a strong effect on the transport characteristics of the original MWCNT. After the break and re-welding, such a defect is taken out of the circuit. Figures 7.4 (c) and (e) also show that the CNT-CNT renewal bonding may be stronger than the bonding at some other weak point elsewhere in the same MWCNT.

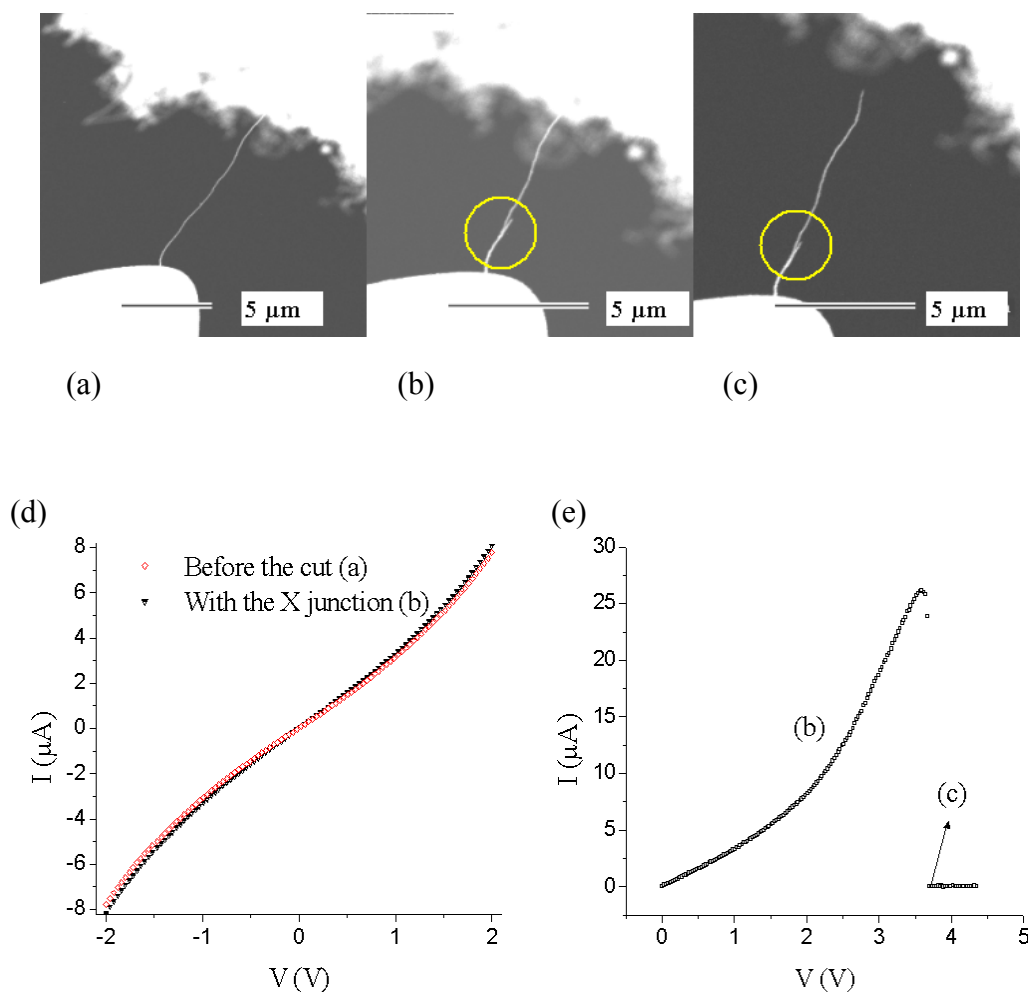Figure 7.4: (a) The MWCNT chosen for the I-V measurement. (b) The X-junction made in the MWCNT. (c) Other weak point breakage caused by increasing the bias. (d) I-V curves of the MWCNT junction. (e) The junction was given a failure test by increasing the bias.

7.3 SUMMARY

X-junctions can be made by cutting the MWCNT and then e-beam welding in the SEM. The I-V curves of the junctions were examined. The MWCNTs normally have

residual defects and impurities so that the current flows not only through the outermost shell but also some the inner metallic tubes of due to scattering. The X-junctions may increase the connection channels between the outermost and the inner shells of the various metallic CNTs. Radial distortion (changes in radius) may also be given along with the formation of X-junctions, which complicates the analysis of the data.

In accordance with the previous work about the ohmic contact between nanotube segments [43] we could also confirm the same behavior in the linear response regime of the low voltage application even only with a mechanical contact between the nanotube segments. It may so happen that some dangling bonds are developed at the cutting edges to form a weak bonding between the cuts. However, without the proper welding the connection was always fragile and would fail with any small external disturbance.

In conclusion the e-beam nano-welding can be applied to make the best available junctions with nanotube segments. The important points here are that the junctions can be made by use of the relatively low energy e-beams of energy in the keV range and the relatively low temperature processing at room temperature. Further studies are required before attempting real integrated circuit applications, where the nano-welding in SEM may also provide the best available guideline for making the nano-electronic circuit connections.

Bibliography

[1] S. Iijima, Nature **354**, 56 (1991).

[2] H. Kroto, J. Heath, S. O'Brien, R.Curl and R. Smalley, Nature **318**, 162 (1991).

[3] M. S. Dresselhaus, G. Dresselhaus, and P. Avouris, *Carbon Nanotubes: Synthesis, Structure, Properties, and Applications*, Springer, New York, 2001.

[4] M. S. Dresselhaus, G. Dresselhaus, R. Saito, Phys. Rev. B **45**, 6234 (1992).

[5] S. Elliott, *The Physics and Chemistry of Solids*, John Wiley & Sons, Chichester, 1998.

[6] A. Bezryadin, A. Verschueren, S. Tans, and C. Dekker, Phys. Rev. Lett. **80**, 4036 (1998).

[7] P. Delaney, H. Choi, J. Ihm, S. Louie, and M. Cohen, Nature **391**, 466 (1998).

[8] X. Blasé, L.Benedict, E. Shirley, and S. Louie, Phys. Rev. Lett. **72**, 1878 (1994).

[9] D. Srivastava, D. Brenner, J. Schall, K. Ausman, M. Yu, and R. Ruoff, J. Phys. Chem. B **103**, 4330 (1999).

[10] NASA Report-Austin Workshop, http://www.ipt.arc.nasa.gov/gallery.html.

[11] M. Di Ventra, S. Evoy and J. R. Heflin Jr., *Introduction to Nanoscale Science and Technology*, Kluwer Academic Publishers, Boston, 2004.

[12] T. Tomaru, Elba 2002 Gravitational Wave Advanced Detector Workshop.

[13] M. Daenen, R. de Fouw, B. Hamers, P. Janssen, K. Schouteden, and M. Veld, *The wondrous world of carbon nanotubes*, 2003.

[14] W. Mizutani, N. Choi, T. Uchihashi, and H. Tokumoto, Jpn. J. Appl. Phys **40**, 4328 (2001).

[15] T. Ebbesen, and P. Ajayan, Nature **358**, 220 (1992).

[16] A. Thess, R. Lee, P. Nikolaev, H. Dai, P. Petit, J. Robert, c. Xu, Y. Lee, S. Kim, A. Rinzler, D. Colbert, G. Scuseria, D. Tomanek, J. Fischer, and R. Smalley, Science **273**, 483 (1996).

[17] A. Melmed, J. Vac. Sci. Technol. B **9(2)**, 601 (1991).

[18] R. Sen, A. Govindaraj, C.N.R. Rao, Chem. Phys. Lett. **267**, 276 (1997).

[19] C. N. R. Rao, R. Sen, B. C. Satishkumar, A. Govindaraj, Chem.Commun. **15**, 1525 (1998).

[20] X. Zhang, A. Cao, B. Wei, Y. Li, J. Wei, C. Xu, D. Wu, Chem. Phys. Lett. **362**, 285 (2002).

[21] Y. Lee, N. Kim, J. Park, J. Han, Y. Choi, H. Ryu, H. Lee, Chem. Phys. Lett. **372**, 853 (2003).

[22] M. C. Schnitzler, M. M. Oliveira, D. Ugarte, and A. J.G. Zarbin, Chem. Phys. Lett. **381**, 541 (2003).

[23] A. Leonhardt, S. Hampel, C. Müller, I. Mönch, R. Koseva, M. Ritschel, D. Elefant, K. Biedermann, and B. Büchner, Chem. Vap. Dep. **12**, 380 (2006).

[24] H. Nishijima, S. Kamo, S. Akita, K. Hohmura, S. Yoshimura, K. Takeyasu and Y. Nakayama, Appl. Phys. Lett. **74**, 4061 (1999).

[25] Z.W. Xu, Q.L. Zhao, T.Sun, L.Q. Guo, J. Mater. Pro. Tech. **190**, 397 (2007).

[26] S. Lu, Z. Guo, W. Ding, D. A. Dikin, J. Lee, and R. S. Ruoff, Rev. Sci. Instr. **77**, 125101 (2006).

[27] W. Mizutani, N. Choi, T. Uchihashi and H. Tokumoto, Jpn. J. Appl. Phys. **40**, 4328 (2001).

[28] K. Kim, S. Lim, I. Lee, K. An, D. Bae, S. Choi, J. Yoo, and Y. Lee, Rev. Sci. Instr. **74**, 4021 (2003).

[29] J. Kim, J. Huang and A. de Lozanne in preparation.

[30] X. Zou, H. Abe, T. Shimizu, A. Ando, H. Tokumoto, S. Zhu, and H. Zhou, Trans. Nonferrous Metals Society of China **16**, 689 (2006)

[31] Y. Simsek, L. Ozyuzer, A. Tugrul Seyhan, M. Tanoglu, K. Schulte, J. Mater. Sci. **42**, 9689 (2007).

[32] L. Langer, V. Bayot, E. Grivei, J.P. Issi, J. P. Heremans, C. H. Olk, L. Stockman, C. Van Haesendonck, and Y. Bruynseraede, Phys. Rev. Lett. **76**, 479 (1996).

[33] V. Semet, V. Binh, D. Guillot, K. Teo, M. Chhowalla, G. Amaratunga, W. Milne, P. Legagneux, and D. Pribat, Appl. Phys. Lett. **87**, 223103 (2005).

[34] C. L. Kane and E. J. Mele, Phys. Rev. Lett. **78**, 1932 (1997).

[35] A. Rochefort, `D. R. Salahub, and P. Avouris, Chem. Phys. Lett. **297**, 45 (1998).

[36] Y. Miyamoto, Phys. Rev. B **54**, R11149 (1996).

[37] E. Minot, Y. Yaish, V. Sazonova, J. Park, M. Brink, and P. McEuen, Phys. Rev. Lett. **90**, 156401 (2003).

[38] T. Tombler, C. Zhou, L. Alexseyev, J. Kong, H. Dai, L. Liu, C. Jayanthi, M. Tang, and S. Wu, Nature **405**, 769 (2000)

[39] M. Terrones, F. Banhart, N. Grobert, J. Charlier, H. terrones, and P. Ajayan, Phys. Rev. Lett. **89**, 075505 (2002).

[40] F. Bussolotti, L. D'Ortenzi, V. Grossi, S. Santucci, and M. Passacantando, Phys. Rev. B **76**, 125415 (2007).

[41] T. Hertel, R. Walkup, and P. Avouris, Phys. Rev. B **58**, 13870 (1998).

[42] A. Sears and R. Batra, Phys. Rev. B **73**, 085410 (2006).

[43] R. Gupta, R. Stallcup II, and M. Panhuis, Nanotech **16**, 1707 (2005).

Vita

Suenne Kim was born in Seoul, Korea on July 4, 1975 as the daughter of Jong-Jean Kim and Young-Sook Hong. She received the Bachelor of Science degree in Physics from the Ewha Womans University, Seoul, Korea and continued her graduate study in physics at the same university to be conferred a Master of Science degree in 2000. Her M.Sc. thesis has the title, "Raman study of an electric field induced and temperature induced phase transition in $Pb(Zn_{1/3}Nb_{2/3})O_3$-8%$PbTiO_3$". After a year of working with the research fellowship award from the Korea Science and Engineering Foundation, she came to the United States to continue her advanced studies for her Ph.D. degree at the Graduate School of the University of Texas, Austin since the Fall semester of 2002, joining the graduate research group of Professor Alex de Lozanne as a research assistant. She has been supported in part by the Ilun Foundation fellowship program of the Jusung Engineering, Ltd. of Korea since 2007.

Permanent address: KIT Apt. 11-205, 236-2 Gajeong-dong, Yuseong-gu, Daejeon 305-350, Korea (Republic of)

This dissertation was typed by the author.